



# Nacre Tablet Thickness Records Formation Temperature in Modern and Fossil Shells

## Citation

Gilbertab, Pupa U.P.A, Kristin D.Bergmann, Corinne E.Myers, Matthew A.Marcus, Ross T. DeVol, Chang-Yu Sun, Adam Z. Blonsky, Erik Tamre, Jessica Zhao, Elizabeth A. Karan, Nobumichi Tamura, Sarah Lemere, Anthony J. Giuffre, Gonzalo Giribet, John M. Eiler, and Andrew H. Knoll. 2017. Nacre Tablet Thickness Records Formation Temperature in Modern and Fossil Shells. Earth and Planetary Science Letters 460: 281-292.

## Permanent link

<http://nrs.harvard.edu/urn-3:HUL.InstRepos:41361258>

## Terms of Use

This article was downloaded from Harvard University's DASH repository, and is made available under the terms and conditions applicable to Open Access Policy Articles, as set forth at <http://nrs.harvard.edu/urn-3:HUL.InstRepos:dash.current.terms-of-use#OAP>

## Share Your Story

The Harvard community has made this article openly available.  
Please share how this access benefits you. [Submit a story](#).

[Accessibility](#)

1  
2  
3  
4  
5  
6  
7  
8  
9  
10  
11  
12  
13  
14  
15  
16  
17  
18  
19  
20  
21  
22

**Nacre tablet thickness records formation temperature  
in modern and fossil shells**

Pupa U.P.A Gilbert<sup>1,2\*</sup>, Kristin D. Bergmann<sup>3,4</sup>, Corinne E. Myers<sup>5,6</sup>, Matthew A. Marcus<sup>7</sup>, Ross  
T. DeVol<sup>1</sup>, Chang-Yu Sun<sup>1</sup>, Adam Z. Blonsky<sup>1</sup>, Erik Tamre<sup>2,3</sup>, Jessica Zhao<sup>2</sup>, Elizabeth A.  
Karan<sup>2</sup>, Nobumichi Tamura<sup>7</sup>, Sarah Lemer<sup>5</sup>, Anthony J. Giuffre<sup>1</sup>, Gonzalo Giribet<sup>5</sup>, John M.  
Eiler<sup>8</sup>, Andrew H. Knoll<sup>3,5</sup>

<sup>1</sup> University of Wisconsin–Madison, Departments of Physics, Chemistry, Geoscience, Madison  
WI 53706 USA.

<sup>2</sup> Harvard University, Radcliffe Institute for Advanced Study, Fellowship Program, Cambridge,  
MA 02138.

<sup>3</sup> Harvard University, Department of Earth and Planetary Sciences, Cambridge, MA 02138.

<sup>4</sup> Massachusetts Institute of Technology, Department of Earth, Atmospheric and Planetary  
Sciences, Cambridge, MA 02139.

<sup>5</sup> Harvard University, Museum of Comparative Zoology and Department of Organismic and  
Evolutionary Biology, Cambridge, MA 02138.

<sup>6</sup> University of New Mexico, Department of Earth and Planetary Sciences, Albuquerque, NM  
87131.

<sup>7</sup> Advanced Light Source, Lawrence Berkeley National Laboratory, Berkeley, CA, 94720, USA.

<sup>8</sup> California Institute of Technology, Division of Geological and Planetary Sciences, Pasadena,  
CA 91125

\* corresponding author, pupa@physics.wisc.edu, previously publishing as Gelsomina De Stasio

23 **Abstract**

24 Nacre, the iridescent outer lining of pearls and inner lining of many mollusk shells, is composed  
25 of periodic, parallel, organic sheets alternating with aragonite ( $\text{CaCO}_3$ ) tablet layers. Nacre tablet  
26 thickness (TT) generates both nacre's iridescence and its remarkable resistance to fracture.  
27 Despite extensive studies on how nacre forms, the mechanisms controlling TT remain unknown,  
28 even though they determine the most conspicuous of nacre's characteristics, visible even to the  
29 naked eye.

30 Thermodynamics predicts that temperature (T) will affect both physical and chemical  
31 components of biomineralized skeletons. The *chemical* composition of biominerals is well-  
32 established to record environmental parameters, and has therefore been extensively used in  
33 paleoclimate studies. The *physical* structure, however, has been hypothesized but never directly  
34 demonstrated to depend on the environment. Here we observe that the physical TT in nacre from  
35 modern and fossil shallow-water shells of the bivalves *Pinna* and *Atrina* correlates with T as  
36 measured by the carbonate clumped isotope thermometer. Based on the observed TT vs. T  
37 correlation, we anticipate that TT will be used as a paleothermometer, useful to estimate  
38 paleotemperature in shallow-water paleo-environments. Here we successfully test the proposed  
39 new nacre TT thermometer on two Jurassic *Pinna* shells. The increase of TT with T is consistent  
40 with greater aragonite growth rate at higher T, and with greater metabolic rate at higher T. Thus,  
41 it reveals a complex, T-dependent biophysical mechanism for nacre formation.

42 **Keywords**

43 Paleo-climate, Proxy, Biomineral, mollusk, PEEM, iridescence.

44

45 **1. Introduction**

46 Calcareous skeletons record animal diversity in marine environments through  
47 Phanerozoic time (<541 Ma) (Alroy et al., 2008; Sepkoski Jr, 1981), and geochemical proxies in  
48 various biominerals document climatic variation through the same interval (Zachos et al., 2001).  
49 The integration of these paleobiological and paleoclimatic records, however, can be challenging  
50 because the skeletal fossils that document animal evolution (Jablonski and Shubin, 2015)  
51 originate mostly from shallow continental shelf and platform environments. In contrast, the most  
52 widely used proxies of marine paleoclimate originate from deep sea sediments, especially for the  
53 record of the last 100 million years when modern ecosystems took shape (Kim et al., 2008;  
54 Zachos et al., 2001). Here we report a promising new paleotemperature proxy stored in the nacre  
55 of bivalve mollusks in the family Pinnidae, which have lived in shallow marine environments for  
56 more than 400 million years. We evaluate this proxy by comparing the physical structure of  
57 nacre (Cartwright and Checa, 2007; England et al., 2007) through geologic time with a  
58 geochemical proxy for temperature: carbonate clumped isotope thermometry (Eiler, 2007).

59 In previous work (Olson et al., 2012) showed that environmental temperature and  
60 pressure might correlate with structural parameters in nacre, but they did so in a broad way,  
61 analyzing shells from eight different nacre-forming species: bivalves, gastropods, and  
62 cephalopods from modern environments. In this work, instead, we analyze bivalves from a single  
63 clade, the family Pinnidae, from modern and ancient shallow shelf environments. This, then, is  
64 the first study to compare, within a single family of bivalves, the potential environmental  
65 controls on nacre tablet thickness.

66 We selected pinnid bivalves for several reasons. Members of the family Pinnidae, or pen  
67 shells, including the genera *Pinna* and *Atrina* (Lemer et al., 2014), are fast-growing sessile  
68 suspension-feeders, widespread in tropical to temperate, coastal, shallow shelf environments,

69 both today and in the past (Aucoin and Himmelman, 2011; Grave, 1911; Richardson et al., 2004;  
70 Schultz and Huber, 2013; Turner and Rosewater, 1958). The pinnid fossil record goes back to the  
71 Silurian Period (~444 Ma) (En-Zhi et al., 1986), and both *Pinna* and *Atrina* have been reported  
72 from Mississippian rocks (359-323 Ma) (Wheelton, 1905) (Figure S1). Their shell morphology is  
73 unique and easily identified, even from fragments. Like many other marine bivalves, pen shells  
74 combine an outer layer of prismatic calcite (CaCO<sub>3</sub>) with an inner nacre layer. Uniquely, their  
75 prismatic calcite and nacre aragonite layers separate easily as the shells dry, providing two  
76 distinct carbonate minerals for clumped isotope analysis. When present in the fossil record,  
77 shells are well-preserved although the prismatic and nacre layers rarely remain attached.  
78 Previous work indicated that bivalves hold promise as temperature proxies (Olson et al., 2012).

79         In this study we quantify the physical parameters of nacre ultrastructure, including nacre  
80 tablet thickness (TT), and compare them to independent estimates of temperature based on  
81 carbonate clumped isotope analysis for both modern and ancient shells of the sister taxa *Pinna*  
82 and *Atrina*. Three modern shells are included, from a range of latitudes and seasonal  
83 temperatures, and nine fossil specimens, drawn from different geologic times, places, and  
84 inferred temperatures. To explore quantitatively the relationship between temperature and nacre  
85 biomineralization, we utilized carbonate clumped isotope thermometry (Eiler, 2007) to compare  
86 independent estimates of paleotemperature with nacre TT for all shells, except for the  
87 diagenetically altered Jurassic specimens. This thermodynamically-controlled, temperature-  
88 dependent geochemical method measures the preferential association of multiple heavy isotopes  
89 within a single carbonate ion ( $\Delta_{47}$ ). Unlike the  $\delta^{18}\text{O}$  paleothermometer, the carbonate clumped  
90 isotope thermometer is independent of the isotopic composition of seawater. Clumped isotope  
91 temperatures for modern shells, when compared to nearby seawater temperatures, are in good

92 agreement, increasing our confidence in clumped isotope paleotemperature estimates from fossil  
93 shells.

94

## 95 **2. Materials and Methods**

96 We obtained fossil shells from various museums (see Supporting Information) and modern shells  
97 from marine biology laboratories. The shells were embedded in EpoFix (EMS, Hatfield, PA) to  
98 prevent damage during cutting, then cut along the bisector line into one half for clumped isotope  
99 and the other half for PEEM analysis. The latter was re-embedded at the center of a 1-inch round  
100 and polished to expose cross-sections and TT, then coated with 1 nm Pt at the center of the  
101 sample, and with a 40 nm Pt frame around it, as described previously (De Stasio et al., 2003;  
102 Gilbert, 2014).

103

### 104 **2.1. PEEM Analysis**

105 A PhotoElectron Emission spectroMicroscopy (PEEM) or PhotoEmission Electron  
106 spectromicroscopy (also PEEM) experiment (Tonner and Harp, 1988) requires a synchrotron —  
107 a *tunable* source of soft-x-ray photons — to produce spectroscopy at the oxygen K-edge, as  
108 shown in Figure 1. It also requires *rotatable* linear polarization, that is, an Elliptically Polarizing  
109 Undulator (EPU) insertion device within the synchrotron, to produce the PIC-maps shown in  
110 Figures 1, 2, 3, 6, S9. PEEM instruments installed on EPU beamlines are common at all  
111 synchrotrons and available free-of-charge to biomineralogists (Gilbert, 2014). For these  
112 experiments we used the PEEM-3 microscope, on beamline 11.0.1, at the Berkeley-Advanced  
113 Light Source.

114 A PEEM produces a magnified photoelectron image of the sample surface as this  
115 photoemits under x-ray illumination. Photoelectron emission, and its variations with incident  
116 energy and polarization, carries information about the chemistry and physical structure of the  
117 sample surface. Scanning the photon energy and acquiring stacks of PEEM images, one can then  
118 extract a spectrum from each image pixel, thus using the PEEM as a spectromicroscope, as in  
119 **Figure 1**. Keeping constant photon energy and scanning the linear polarization angle while  
120 acquiring a stack of PEEM images, one can extract a polarization spectrum. This can then be  
121 used to reconstruct the crystal orientation for each pixel, resulting in the use of PEEM as a PIC-  
122 mapper (e.g., **Figure 1, 2, 3, 6, S9**). Both modes of data acquisition, spectroscopy and PIC-  
123 mapping, are described below.

124

## 125 **2.2. O spectroscopy Analysis**

126 The spectra in **Figure 1**, and other regions of modern and fossil shells, were obtained using X-ray  
127 Absorption Near-Edge Structure (XANES) spectroscopy at the O K-edge. All spectra were  
128 extracted from stacks of images and normalized using GG Macros ([GG-Macros, 2016](#)). Oxygen  
129 spectra from shells were extracted from stacks of 181 images,  $20\ \mu\text{m} \times 20\ \mu\text{m}$  or  $55\ \mu\text{m} \times 55\ \mu\text{m}$   
130 in size, with  $10^6$  pixels each, acquired across the O K-edge between 525 and 555 eV. The energy  
131 step was 0.1 eV in the most relevant fine structure region (530-545 eV), and 0.5 eV step in the  
132 relatively featureless pre- and post-edge spectral regions.

133 The presented spectra were acquired with vertical polarization from the EPU, so polarization-  
134 dependent intensity of peaks (most prominently the  $\pi^*$  peak at 534 eV) can be observed to vary  
135 depending on crystal orientation. These oxygen spectra were acquired binning  $31 \times 31$  pixel

136 spectra, each 55 nm in size, hence each spectrum originated from a  $1.705 \mu\text{m} \times 1.705 \mu\text{m}$  square,  
137 in the locations indicated in [Figure 1](#).

138 The spectra were normalized to a beamline  $I_0$  acquired on the thick Pt region of each  
139 sample, also with vertical polarization. To normalize, the pre-edge of the O spectrum was  
140 aligned to the pre-edge (525-532 eV) of the  $I_0$ , then the O spectrum was divided by the  $I_0$ . After  
141 normalization, all O spectra in [Figure 1](#) were scaled to intensities of 0 at 525 eV and 1 at 535 eV.  
142 Aragonite spectra were displaced up, and organics and epoxy spectra displaced down, for clarity.  
143 Note that the spectra in [Figure 1](#) are shifted in energy so that the  $\pi^*$  peak is at 534 eV, following  
144 Stohr's classic article on carbonates ([Madix et al., 1988](#)). As first described by DeVol et al.  
145 ([DeVol et al., 2014](#)), aragonite and calcite spectra have distinct spectra at the O K-edge.  
146 Aragonite exhibits six peaks, and calcite four peaks, marked by thin black vertical lines under  
147 each peak in [Figure 1](#). The first peak at 534 eV is an  $O_{1s \rightarrow \pi^*}$  transition peak associated with the  
148 carbonate C—O bond (hereafter termed  $\pi^*$  peak), which is most sensitive to the crystal  
149 orientation direction, the second peak is associated with the O—Ca bond and is polarization-  
150 independent, the other peaks are from the carbonate C—O bond and have  $O_{1s \rightarrow \sigma^*}$  character (  $\sigma^*$   
151 peaks), thus they are anti-correlated with the  $\pi^*$  peak. In [Figure 1](#) it is evident that in each  
152 spectrum when the  $\pi^*$  peak is high the  $\sigma^*$  peaks are low, and vice versa.

153

### 154 **2.3. PIC-mapping**

155 A stack of 19 images was acquired for each Polarization-dependent Imaging Contrast (PIC)-map  
156 ([DeVol et al., 2014](#); [Gilbert et al., 2011](#); [Metzler et al., 2007](#); [Metzler et al., 2008](#)). In these  
157 images the photon energy was fixed at the oxygen K-edge  $\pi^*$  peak, which is a sharp, intense  
158 peak at 534 eV extremely sensitive to polarization in carbonates ([Figure 1 spectra](#))([DeVol et al.,](#)

159 [2014](#)). The linear polarization angle was then rotated by 90° (from horizontal to vertical) in 5°  
160 steps. PIC-maps were produced from the stack of 19 polarization images using the Polarization  
161 Analysis Package (part of the Gilbert Group Macros, run in Igor Pro Carbon<sup>®</sup>). This software for  
162 PC or Mac can be downloaded free of charge from ([GG-Macros, 2016](#)).

163 Detailed descriptions of PIC-mapping from stacks of polarization images were previously  
164 published ([DeVol et al., 2014](#); [Gilbert et al., 2011](#); [Olson et al., 2013](#); [Olson et al., 2012](#)).

165 Briefly, the intensity vs. polarization angle  $\chi$  curve from each pixel is fit to

$$166 \quad f(\chi) = a + b \cos^2(\chi - c'), \quad (\text{Equation 1})$$

167 where  $a$ ,  $b$ ,  $c'$  are fit parameters. The colors produced in PIC-maps describe the angle of the  
168 projection of the  $c$ -axis onto the polarization plane, termed  $c'$ -axis. When this axis is vertical (in  
169 the laboratory and in the images), the angle is 0° and the color is cyan, when the  $c'$ -axis is  
170 horizontal left (-90° from the vertical) and right (+90°), the color is red; intermediate colors  
171 follow the legend in [Figures 1-3](#). Color PIC-maps also show with brightness the  $c$ -axis  
172 orientation off-plane (polarization plane): bright colors indicate in-plane  $c$ -axes, darker colors are  
173 off-plane, and black is 90° off-plane (that is, the  $c$ -axis is pointing directly into the x-ray beam)  
174 ([DeVol et al., 2014](#)). For all PIC-maps presented here, the default ([GG-Macros, 2016](#)) parameter  
175 values were used: angle minimum = -90, maximum +90, scalebar colors 0°-360°, brightness set  
176 to max B = 200.

177 Approximately 1000 PIC-maps were produced, including some replicates. Replicates from the  
178 same position provided identical results, but were excluded from TT and angle spread  
179 measurements since they are not independent measurements. Excluding replicates, the number of  
180 PIC-maps in which we measured TT is 842, and these are all shown in [Figure 6](#), but we only  
181 obtained clumped isotope data from nine shells, hence the TT data in [Figures 7 and S10 and](#)

182 **Table S4** only include TT measurements from 630 PIC-maps. Once a color PIC-map is produced  
183 by the GG Macros, transects of partly overlapping PIC-maps were composed in Adobe  
184 Photoshop<sup>®</sup> and presented in **Figure 6**.

185

#### 186 **2.4. TT measurements**

187 **Figure S10** illustrates the average TT measured in each PIC-map in each series across the  
188 thickness of each of the twelve analyzed shells. In order to measure the average TT of each PIC-  
189 map, we divided the number of layers by the vertical size of the field of view (vertical-FoV) in  
190 each PIC-map. The vertical-FoV was nominally 20  $\mu\text{m}$ , but the experimentally measured FoVs  
191 varied slightly across samples from 20.5  $\mu\text{m}$  to 22.2  $\mu\text{m}$ . For the two Jurassic *Pinna* samples we  
192 operated in “large FoV” mode, hence the dark edges in each image in the transect on the right  
193 hand side of **Figure 6**. For the 20 PIC-maps from Jurassic Pfo1-3 and Ps8-2 the FoV was 63.6  
194  $\mu\text{m}$  and 61.3  $\mu\text{m}$ , respectively.

195 To identify the number of layers in the 822 PIC-maps with 20- $\mu\text{m}$  FoV we used a digital  
196 ruler as shown in **Figure S9**. This method is less error-prone than other methods we explored.  
197 Automated layer counting was discarded because two different software approaches generated  
198 frequent false positives and false negatives. The digital ruler is different from a physical ruler in  
199 that the position of each tick mark is not fixed but is moved vertically, independently from all  
200 others, to coincide with the boundary between two nacre tablets. This results in tick marks  
201 manually positioned along all nacre tablet boundaries within each PIC-map. Thus the vertical  
202 distance between ticks varied by TT, but the sequence of ticks and their corresponding numbers  
203 never changed. This scheme facilitated accurate counting of the number of layers per PIC-map,  
204 and enabled efficient independent measurement and cross-checking by multiple authors. The

205 average TT in each PIC-map was calculated by dividing the vertical field of view by the number  
206 of tablets counted using the digital ruler.  
207 Across the 822 images analyzed, the number of nacre tablet layers varied from 21—87, and the  
208 average TTs varied from 0.253 — 1.057  $\mu\text{m}$ . As an example, in [Figure S9](#) there are 42, 37, 27,  
209 26 tablets, respectively, and the vertical-FoV was measured as 21.5  $\mu\text{m}$  in all maps. Thus, the  
210 average TT calculated for these PIC-maps was 0.512  $\mu\text{m}$ , 0.581  $\mu\text{m}$ , 0.796  $\mu\text{m}$ , and 0.827  $\mu\text{m}$ ,  
211 respectively. The error assigned to each measurement was between one and five tablets,  
212 depending on the image quality, the sample preservation, and the resulting level of confidence in  
213 the measurement.

214 In fossil shells, a gap is occasionally observed between nacre tablets ([Figure 2](#)). Gaps  
215 may represent the approximate thickness of one nacre tablet or many. In all cases when gaps  
216 were encountered, the spacing of tick marks in the digital ruler below and above the gap were  
217 used to estimate the number of missing tablets. Thus, gaps were artificially filled with tablets.  
218 This enabled us to maintain continuity of the measured coordinates in the PEEM specimen, and  
219 keep track of where each PIC-map was located in space and time. It cannot be determined if the  
220 gaps were the result of dissolution of some tablets, or mechanical separation of previously  
221 adjacent tablets. The approach of filling the gap with virtual tablets (digital ruler tick marks)  
222 assumes the former scenario. Should this assumption be wrong, the error introduced is  
223 negligible: on the order of 10-50  $\mu\text{m}$  per shell (with the exception of specimen Ah3, which has a  
224 300- $\mu\text{m}$  gap).

225

## 226 **2.5. Jurassic Pinna TT measurements**

227 Since the 20 PIC-maps from Jurassic *Pinna* shells were acquired with larger FoV and the shells  
228 were poorly preserved, we could not use the digital ruler, nor any other automated measuring  
229 tool. We therefore measured each tablet thickness individually, using ImageJ<sup>®</sup> 1.49v. For this  
230 purpose, we first set the scale in ImageJ, then defined a series of numbered dots at the top and  
231 bottom of sufficiently well-preserved tablets, which could provide reliable TT. The numbered  
232 dots were produced using the multi-point tool. We then used the length tool to measure the  
233 distance between each pair of subsequent dots, in precisely the same order as the numbered dots,  
234 so the measurement was reproducible by two co-authors. We then exported all measured  
235 distances and processed them in Microsoft Excel<sup>®</sup> and Kaleidagraph<sup>®</sup> 4.5 as all other data.

236

## 237 **2.6. Carbonate Clumped Isotope Analysis**

238 The clumped isotope thermometer measures the preferential association (termed  $\Delta_{47}$ ) of  
239 two heavy isotopes, <sup>13</sup>C and <sup>18</sup>O, with a light <sup>12</sup>C to form heavy CO<sub>2</sub> molecules originating from  
240 carbonate ions, which is T-dependent, and it does not require knowledge of the seawater in  
241 which the animal lived when it formed its shell.

242 Because 8-10 mg of carbonate is required for a single analysis, we sampled aragonite and  
243 calcite phases close to the PIC-mapped region (either immediately adjacent in the same valve or  
244 across from it in the same location but on the opposite valve; the latter was only done for Ar5  
245 samples, calcite and aragonite). The Ar5 data are not included, due to significant organic  
246 contamination during analysis despite multiple attempts to clean and reanalyze the sample. The  
247 shell material was separated first by saw and then by hand from the majority of the epoxy resin.  
248 Epoxy did not fully penetrate the nacre tablets which allowed the nacre to be split along planes  
249 of weakness. A subset of samples were separated for clumped isotopes before embedding. For

250 all shells sheets of nacre were harvested and powdered in a mortar and pestle. Samples of 8-12  
251 mg of powder were weighed into silver capsules before being reacted at 90°C in 100% H<sub>3</sub>PO<sub>4</sub> in  
252 a common acid bath. Evolved CO<sub>2</sub> was purified by multiple cryogenic traps including a  
253 Porapak-Q chromatograph held at -20°C before being analyzed (Eiler, 2007; Passey et al., 2010).  
254 The abundance of “doubly substituted” molecules with <sup>13</sup>C and <sup>18</sup>O are measured as mass 47  
255 CO<sub>2</sub> after phosphoric acid digestion of the carbonate along with mass 44, 45 and 46 CO<sub>2</sub> on a  
256 Thermo Scientific MAT 253 IRMS (Eiler, 2007; Passey et al., 2010). All samples were prepared  
257 at the California Institute of Technology and analyzed during two analytical sessions in February  
258 2015 at the California Institute of Technology, and in June 2015 at the Massachusetts Institute of  
259 Technology. Samples run at the Massachusetts Institute of Technology in June 2015 were  
260 prepared through the automated cryogenic trap setup at the California Institute of Technology  
261 before being stored in sealed quartz tubes for later analysis. Methods for the measurement and  
262 corrections to analyzed heated gases run during each session follow those of (Huntington et al.,  
263 2009). Δ<sub>47</sub> values were transformed into an absolute reference frame using an empirical transfer  
264 function following (Dennis et al., 2011) based on two compositions each of 25°C equilibrated  
265 CO<sub>2</sub> gas and 1000°C heated CO<sub>2</sub> gas. Finally Δ<sub>47</sub> values for carbonate samples were corrected  
266 by +0.092‰ for the 90°C acid bath reaction temperature within the absolute reference frame  
267 (Henkes et al., 2013).

268 Values within the carbon dioxide equilibrium scale (CDES) for two internal standards  
269 used over the course of the analyses, CIT Carrara and TV03 were calculated from weeks when  
270 1000°C CO<sub>2</sub> was analyzed daily and 25°C CO<sub>2</sub> gases were analyzed bi-weekly. The calculated  
271 values for the two standards in the CDES are reported with 1 SD for all sessions with heated

272 gases and equilibrated gases: CIT Carrara  $\Delta_{47}$ -CDES =  $0.737 \pm 0.2$  ‰ ( $1\sigma$ ,  $n = 12$ ), TV03  $\Delta_{47}$ -  
273 CDES =  $0.421 \pm 0.012$ ‰ ( $1\sigma$ ,  $n = 10$ ).

274 For single unknown measurements the uncertainty of the measurement is reported as the  
275 standard error of the mean (S.E.M.) of  $\Delta_{47}$  measurements over 8 acquisition cycles, with 7  
276 measurements for each cycle. For replicate measurements  $n \geq 2$ , the error is reported as the  
277 S.E.M. of  $\Delta_{47}$  over the number of sample replicates.

278 Temperatures were calculated in the absolute reference frame using a recent mollusk  
279 (aragonite and calcite) and brachiopod (calcite) calibration that utilized a nearly identical  
280 cryogenic preparation setup at JHU (Henkes et al., 2013). Mineral  $\delta^{18}\text{O}_{\text{VPDB}}$  was calculated  
281 using aragonite and calcite specific acid fractionation factors for a 90°C reaction (Kim et al.,  
282 2007a; Kim and O'Neil, 1997). Water  $\delta^{18}\text{O}_{\text{VSMOW}}$  was calculated from the clumped isotope  
283 temperature and mineral  $\delta^{18}\text{O}_{\text{VPDB}}$  using mineral-water specific fractionation factors for  
284 aragonite and calcite (Kim and O'Neil, 1997; Kim et al., 2007b).

285 All clumped isotope data are presented in Table S2.

286

## 287 **2.8. Plots and Linear Fits**

288 All plots presented were produced using Kaleidagraph<sup>®</sup> 4.5.2 for Mac. In Figure 7B the  
289 correlation of TT and T, and in Figure 10 the correlation of particle size and T were tested in  
290 Kaleidagraph<sup>®</sup> using the “Linear” “Curve Fit” function. The goodness of the fit was estimated by  
291 the correlation coefficient R produced along with the fit. Notice that the linear fit did not take  
292 into account the error bars. For this reason we only used this simple linear fit in Figures 7B and  
293 10, where we obtained correlation coefficients  $R = 0.98$  and  $R=0.97$ , respectively.

294

295           The bootstrapping method we used to obtain the relationship of mean TT vs T in each  
296 image (Figure 7A), however, is far more accurate, includes all errors, and is statistically more  
297 significant and informative, as described below.

298           In Figure 7A, in order to estimate the proper fit “line” and its errors in the presence of  
299 error bars in both T and TT, it was necessary to consider carefully the statistics of the data. For  
300 each shell, there was uncertainty in both the ‘measured’ and ‘known’ temperatures from  
301 clumped-isotope measurement error as well as seasonal variations at a given site. For each shell,  
302 there were many measurements of TT, each of which had a relatively small error bar, but which  
303 varied quite a bit within a shell's data-set. This is why Figure 7A shows the data for each shell as  
304 a vertical cloud of points. To figure out error bars when the “line” is used as a thermometer, we  
305 consider what happens if we take one TT measurement per shell, and run a fit line through the  
306 resulting 9 points. Figure S12 shows what we did for each such trial, with one data point per  
307 shell, and its vertical and horizontal error bars. We then repeated 100,000 times, each time  
308 randomly selecting 1 datapoint per shell and doing a linear fit through the 9 points. In order to  
309 account for the error bars in our estimates of the statistics of the fits, we added Gaussian random  
310 deviates to displace each point within the box defined by its error bars, with standard deviations  
311 given by the error bars. This displacement is shown by the black arrows in Figure S12 displacing  
312 the green dots to the magenta dots. We then fit a line through the magenta dots (magenta line).  
313 Doing this 100,000 times led to a thicket of lines for which the centroid (blue line) is the  
314 unbiased estimate. The confidence limits are evaluated by looking for the 90<sup>th</sup> and 50<sup>th</sup> percentile  
315 values of the fitted  $y$  for given values of  $x$  (light blue hyperbolae). The distributions we find for  
316 the 100,000 fit coefficients (slope and intercept) are symmetrical, therefore the mean and median  
317 fit lines at each point are the same, and the unbiased estimate is also the most probable value.

318 However, the distributions have wider tails than Gaussian, so the 95% confidence bands are  
319 wider compared with the 90% bands than would be expected from Gaussian distributions.

320 In order to perform the fit with correct weighting, we had to use a linear-fit method that  
321 takes into account error bars on both coordinates. One such method is described in ref. (Press et  
322 al., 1996). The least-squares method without errors in the independent variable amounts to  
323 minimizing

$$324 \quad S = \sum_{i=1}^N ((y_i - a - bx_i) / \sigma_i)^2 \quad (\text{Equation 2})$$

325 with respect to the coefficients  $a$ ,  $b$ , where  $x_i$ ,  $y_i$ , with  $i=1\dots N$ , are the coordinates of the  $N$  data  
326 points and  $\sigma_i$  are the  $y$ -axis error bars. The generalization to the case of  $x$ -axis errors is to define  
327 the sum-square error as:

$$328 \quad S = \sum_{i=1}^N \frac{(y_i - a - bx_i)^2}{\sigma_{yi}^2 + b^2 \sigma_{xi}^2}. \quad (\text{Equation 3})$$

329 This function reduces to Equation 2 for the no- $x$ -error case and is also invariant under rescaling  
330 of the coordinates. It is easy to solve analytically for the value of  $a$  that minimizes  $S$  for a given  
331  $b$ , but the same is not true for  $b$ . Therefore, a golden-section search was performed in order to  
332 solve for  $b$ .

333 It could be argued that we are taking the errors into account twice, thus overestimating  
334 their effect. Indeed we do use the errors in two places, once to displace the data point position  
335 within its error bars, and again to do the generalized least-squares fit. The latter essentially  
336 weights the points correctly according to their reliability. We want the data from a shell to count  
337 for less if the temperature is very uncertain than if it is precisely known. However, that can't be  
338 the whole story. It is obvious from Equation 3 that if all errors in  $x$  and  $y$  are, say, doubled, then

339 the fit coefficients are unaffected, but certainly the fit estimate becomes less reliable. The theory  
340 of error estimation in ordinary linear-least-squares fitting essentially amounts to asking what  
341 happens to the fit line if the data are off by random amounts with standard deviations given by  
342 the  $1\sigma$  error bars. Because the fits we do are more complex than ordinary least-squares fitting,  
343 we don't attempt analytic solution but instead use computation to get the distribution of errors.  
344 This yields the most reliable results, and can more accurately and reliably be used by future users  
345 of the nacre TT thermometer.

346

## 347 **2.9. Jurassic Pinna T measurements**

348 In order to measure the formation T for the two Jurassic *Pinna* samples using the TT  
349 thermometer, we did the following. To measure the T in Kaleidagraph<sup>®</sup> 4.5 we plotted the graph  
350 up to 50°C, magnified it 400%, plotted all lines as hairlines and plotted the measured TT values  
351 as horizontal black lines (also shown in Figure 7A). We then used the coordinates-measuring  
352 tool to identify where the horizontal black lines intersected the line, and the confidence level  
353 curves, to provide T and its errors.

354 Additional methods are described in the Supporting Information, including sample  
355 acquisition and preparation, XRD, SEM, and EPMA analysis, a detailed description of digital  
356 ruler and angle spread measurements, and the abiotic aragonite growth experiment.

357

### 358 3. Results and Discussion

#### 359 3.1. Tests for Diagenetic Alteration

360 If nacre is to provide a reliable indication of ancient shallow water temperatures, we must first  
361 demonstrate that it can be preserved intact over long time intervals. Figure 1 shows PEEM  
362 results for both PIC-mapping (DeVol et al., 2014; Gilbert et al., 2011; Metzler et al., 2007;  
363 Metzler et al., 2008) and x-ray absorption spectra at the oxygen K-edge (DeVol et al., 2014), for  
364 modern, Cretaceous, and Jurassic shells. The modern and Cretaceous specimens are essentially  
365 identical, documenting mineralogical and crystallographic preservation on nearly 70 million year  
366 timescales, consistent with previous results on the organic and mineral components (Weiner et  
367 al., 1976). The Jurassic specimen shows clear signs of diagenesis, with only few tablets  
368 preserved. For the modern and Cretaceous shells, x-ray absorption spectra (Figure 1D) extracted  
369 from microscopic areas of aragonite and calcite are identical to those from their geologic and  
370 synthetic counterparts, exhibiting 6 and 4 peaks, respectively (DeVol et al., 2014). We note that  
371 in PIC-maps of nacre, provided nacre is mounted as all samples in this work, with nacre layers  
372 horizontal, nacre tablets have their c-axes either vertical, with  $0^\circ$  c'-axis angle, which is  
373 displayed as cyan in a PIC-map, or nearly vertical, within  $\pm 15^\circ$  (Olson et al., 2013), which is  
374 displayed between bluish-cyan and greenish-cyan. We will refer to this range of colors as  
375 turquoise. Thus, simply using the color in PIC-maps, one can tell at a glance if nacre is well  
376 preserved and maintains its turquoise orientation, or if it has recrystallized to different  
377 orientations, as observed extensively in Jurassic *Pinna* shells, and sporadically in Modern-  
378 Cretaceous shells.

379 X-ray micro-diffraction of both Cretaceous shells confirms that nacre and prismatic  
380 layers remain aragonite and calcite, respectively, as deposited by the animal (Figure S2).

381 Electron Probe Micro-Analysis (EPMA) measurements show trace concentrations of Mg, Sr, Fe,  
382 Mn, and S, which are typical of aragonite and calcite, respectively, and thus confirm excellent  
383 preservation of one of the Cretaceous shells (Figure S3, Table S3). Fe and Mn trace metal  
384 concentrations are extremely low across the shell (aragonite [Fe] =  $110 \pm 12$  ppm and [Mn] =  $90$   
385  $\pm 10$  ppm; calcite [Fe] =  $202 \pm 42$  ppm and [Mn] =  $93 \pm 27$  ppm) and Sr and Mg are consistent  
386 with primary formation of the two phases from seawater (aragonite [Sr] =  $2567 \pm 71$  ppm and  
387 [Mg] =  $134 \pm 33$  ppm; calcite [Sr] =  $986 \pm 38$  ppm and [Mg] =  $3909 \pm 187$  ppm).

388  
389 Thus, in addition to O spectroscopy and PIC-mapping, crystallographic and chemical  
390 analyses confirm excellent preservation of Modern-Cretaceous shells, with minimal diagenetic  
391 alteration of crystal structure in these and most other areas of the fossil shells. Diagenetic change  
392 was observed sporadically in the PIC-maps of Eocene and Cretaceous specimens, predominantly  
393 near cracks where water presumably penetrated, dissolved and re-precipitated aragonite (sic!)  
394 crystals with greater-than-normal angle spreads in c-axis orientation. Out of 822 PIC-maps  
395 acquired in all Modern-Cretaceous shells, only 6 exhibit signs of diagenesis, and all of these are  
396 shown in Figure 2. Major but still incomplete diagenesis was observed in the Jurassic specimens  
397 as shown in Figures 1C and 2F, where calcite was re-precipitated.

398  
399 **3.2. Nacre tablet thickness in modern and ancient shells**  
400 Figure 3 shows typical PIC-maps of shells from each of the five geologic epochs in this study:  
401 modern, Miocene, Eocene, Late Cretaceous, and Early Jurassic. The PIC-maps of Figure 3 show  
402 that each aragonite tablet behaves as a single crystal and is similar in orientation, within  $\pm 15^\circ$ , to  
403 other tablets, all of them turquoise. This is consistent with previous observations in modern nacre

404 (England et al., 2007; Olson et al., 2013). Tablet layers are interspersed with 30nm-thick organic  
405 sheets (Levi-Kalisman et al., 2001), visible as black lines in Figure 3A,B but not always  
406 preserved in fossils (Figure 3C,D). The orientation-color contrast, therefore, enables  
407 identification of individual tablets even where organics are absent, e.g., in the blue tablets below  
408 the word “Eocene” in Figure 3C. This enables the observation and measurement of TT in  
409 samples of variable preservation and age.

410         The complete data set in this work is presented in Figure 6. This includes three modern  
411 (Figures 4, 5, S4) and nine fossil pen shells (Figures S5-S8), analyzed with a continuous series  
412 of partly overlapping PIC-maps forming a transect across nacre, acquired in the same location in  
413 the shell, that is, the thickest nacre region magnified in Figure 5 and indicated by red arrows in  
414 Figures 4, S4, S7. The average TT in each image was measured by dividing the vertical field of  
415 view of that image by the number of tablet layers present, counted digitally, as shown in Figure  
416 S9 and described in the methods and more in detail in the Supporting Information. In Figure S10  
417 we present the results of all TTs in each shell cross-section, which shows the variability of TT  
418 through time as nacre is deposited.

419

### 420 **3.3. Clumped Isotope Temperature Estimates**

421 First, we validated the clumped isotope thermometer by comparing its results in two modern  
422 shells collected from locations with known water temperature. As shown in Figures 8, 9, the  
423 agreement is good. Given the likelihood that the transect near the umbo in these two shells was  
424 formed over less than a year (Aucoin and Himmelman, 2011) deviations from the mean annual  
425 temperature are not surprising. In both Figures 8 and 9 there is significant overlap between  
426 clumped isotope measurements in the shells and the independently measured water temperature

427 in the locations of their formation. Calculated  $\delta^{18}\text{O}_{\text{VSMOW}}$  values of precipitating seawater are  
428 positive and similar to measured  $\delta^{18}\text{O}_{\text{VSMOW}}$  data from the Gulf of Mexico, Mediterranean Sea  
429 and tropical Caribbean Sea, which are evaporatively enriched in heavy isotopes (Table S2). The  
430 good agreement of clumped isotope T and water T stimulated us to complete carbonate clumped  
431 isotope analyses on Miocene, Eocene and Cretaceous specimens.

432 For fossil shells, reconstructed paleotemperatures appear reasonable given their  
433 paleolatitudes and predicted climatic trends from other proxies (Zachos et al., 2001). The  
434 Miocene specimen mean temperature estimates ( $3 \pm 4^\circ\text{C}$ ,  $12 \pm 2^\circ\text{C}$ ,  $22 \pm 3^\circ\text{C}$ ) sit within the  
435 current range of seasonal temperatures from the Chesapeake Bay and Mid-Atlantic Coast. The  
436 Eocene specimens yield higher temperatures ( $16 \pm 2.5^\circ\text{C}$  and  $21 \pm 5^\circ\text{C}$ ), and the Cretaceous  
437 paleotemperature estimates ( $23 \pm 3^\circ\text{C}$  and  $27 \pm 4^\circ\text{C}$ ) are warmest and most similar to the modern  
438 specimen from tropical Panama.

439 The Jurassic specimens were not analyzed, as extensive diagenesis made bulk analysis  
440 meaningless. Reconstructed paleotemperatures for the fossil shells are consistent with T  
441 estimates for the Miocene mid-Atlantic coast and Eocene and Cretaceous Gulf Coast from other  
442 proxies (Rosales et al., 2004; Zachos et al., 2001). For modern shell Ar5 we have TT  
443 measurements in Figure S10 and water T measurements in Figure S11, but not clumped isotope  
444 temperatures due to severe organic contamination of the sample. Unlike the other modern and  
445 ancient samples Ar5 is a very thick shell with abundant recalcitrant organic material.

446

#### 447 **3.4. Nacre Tablet Thickness Quantitatively Reflects Temperature**

448 Figure 7A shows the observed strong correlation of TT with formation T. In each of the pen  
449 shells, Modern-Cretaceous, mean T from clumped isotopes was measured along with average TT

450 in each PIC-map across the entire thickness of nacre. All measurements and all error bars, from  
451 each specimen were used (630 PIC-maps total) to examine the relationship between TT and T.  
452 The most probable linear fit between TT and T, and its confidence level (CL) intervals were  
453 determined using one randomly selected data point per shell, randomly positioned within its error  
454 bars, then linear-fitting the 9 points, and repeating 100,000 times (Figure S12). Neglecting all  
455 error bars and averaging all data, which is less accurate but frequently done, gives a linear fit  
456 with  $R = 0.98$  ( $R^2 = 0.96$ ), as shown in Figure 7B. The observation of such a strong correlation  
457 between mean TT and mean T, despite fluctuations in each shell (some strong, as in Px1,  
458 discussed below) (Figure S10), indicates that nacre preserves a physical record of carbonate  
459 formation temperature. As noted, each shell displays a range of TT values depending on the  
460 location within the shell transect where the measurement was taken, and may reflect the  
461 contribution of other underlying physical factors, but the average value of the TT distribution  
462 clearly shows a shift to higher value with temperature (Figure 7). For each shell, we have  
463 therefore taken TT measurements in complete transects to account for the intrinsic fluctuations in  
464 TT.

465         The empirical observation that TT and T are highly correlated may be due to several  
466 factors, including metabolic rate, which increases with T (Gillooly et al., 2001). Greater  
467 metabolic rate increases all biological activities, including synthesis and transport of nacre  
468 precursor phases (DeVol et al., 2015), polysaccharides, and proteins to forming nacre. In  
469 addition, a simple experiment in the absence of any organics confirms that the kinetics of crystal  
470 growth may also affect TT. We measured abiotic aragonite growth rates at different temperatures  
471 over a standard time range. The results confirm a linear, positive correlation of particle size with  
472 T, with a correlation coefficient  $R = 0.97$  ( $R^2 = 0.94$ ), as presented in Figure 10. Importantly, the

473 correlation is positive in both Figures 7 and 10; thus, crystal growth rate and metabolic rate may  
474 both contribute to TT, and both are sensitive to T in the same direction: they increase with T. The  
475 slope of the linear fit is more than 100-fold greater in abiotic versus biotic growth ( $1.5311 \mu\text{m}/^\circ\text{C}$   
476 in synthetic aragonite vs.  $0.0144 \mu\text{m}/^\circ\text{C}$  in pen shells, Figures 10 and 7); hence, the temperature-  
477 sensitivity of aragonite growth rates for nacre deposition in animals is much weaker than for  
478 crystal growth from solution. Importantly, the correlation is positive in both Figures 7 and 10.  
479 Thus the correlation between nacre tablet thickness and temperature observed in Figure 7 may  
480 reflect greater growth rate or final crystal size at higher temperature, modified but not obscured  
481 by physiology.

482         Within a shell, we sometimes see large fluctuations in the local TT as a function of  
483 position. For instance, using the TT vs. T equation to measure temperature vs. position for shell  
484 Px1-1 in Figure 7 and Figure S10, the minimum and maximum T obtained are unrealistically low  
485 and high, respectively, at  $2^\circ\text{C}$  and  $50^\circ\text{C}$ . These fluctuations may be due to factors other than T  
486 that affect TT: possibly salinity, pH, or nutrients. The extreme end-member TTs, however, are  
487 averaged out in the all-inclusive analysis, which is precisely what is observed in the average  
488 linear fit of Figure 7A or the linear fit of the averages in Figure 7B. This suggests that despite the  
489 influences of other factors, temperature has an overarching role in determining nacre tablet  
490 thickness. A similar behavior is observed in foraminifera and T estimates from  $\delta^{18}\text{O}$ , which  
491 exhibit out of range values locally, that are averaged out across the entire shell (Kozdon et al.,  
492 2009; Rollion-Bard et al., 2008).

493         Finally, we used the TT vs. T relationship observed here to estimate the T of formation  
494 for Jurassic *Pinna* shells, measuring TT in the few well-preserved tablets, shown as horizontal  
495 black lines in Figure 7A. Two transects from the Pfo1 shell provide very similar most-probable

496 temperatures,  $T=23^{\circ}\text{C}$  and  $21^{\circ}\text{C}$  respectively, whereas for the Ps8 shell we obtained  $T=14^{\circ}\text{C}$ .  
497 50% confidence levels (CL) are:  $21\text{-}27^{\circ}\text{C}$  and  $19\text{-}24^{\circ}\text{C}$  for Pfo1,  $12\text{-}16^{\circ}\text{C}$  for Ps8; 90% CL are:  
498  $18\text{-}34^{\circ}\text{C}$  and  $16\text{-}31^{\circ}\text{C}$  for Pfo1,  $8\text{-}20^{\circ}\text{C}$  for Ps8. All three temperatures are consistent with  
499 expected T values for the Early Jurassic (Rosales et al., 2004). From these estimates, the shell  
500 transects (away from the umbo) are likely to have formed in a Jurassic summer and winter,  
501 respectively. Notably, diagenesis had made these Jurassic shells inaccessible to most chemical  
502 proxies, but left them within reach for the nacre TT thermometer.

503

#### 504 **4. Conclusions**

505 The physical structure of biominerals has seldom been related to environmental parameters.  
506 Olson et al. (Olson et al., 2012) hypothesized that nacre ultrastructure may depend on  
507 environmental temperature at the time of biomineral deposition. Other authors confirmed that  
508 other physical parameters in bivalves (Milano et al., 2015; Schöne et al., 2002) and in  
509 foraminifera (Be, 1968; Frerichs et al., 1972) correlate with temperature. Here we demonstrated  
510 that pen shells record and preserve a quantitative indication of average temperature in the  
511 thickness of nacre tablets formed during shell growth, thus providing a new physical proxy for  
512 paleo-temperatures. We tested the nacre TT thermometer on two Jurassic *Pinna* shells not  
513 accessible to other proxy methods.

514

515 Here TT was measured in PIC-maps; however, SEM images can provide quick and easy access  
516 to the required TT data. Assuming that mean annual temperatures are stable over a period of time,  
517 with the future measurement of many shells all representing the same period, then the mean T-  
518 value will average out the fluctuations of all variables other than T that contribute to TT, if any.

519 With additional TT data from many samples, therefore, the accuracy of the nacre TT proxy will  
520 increase.

521 All paleoenvironmental proxies have their strengths and weaknesses, but temperature  
522 estimates from nacre TT are more forgiving than many, simply requiring good preservation of a  
523 series of aragonite tablets even when other regions of the shell experienced dissolution,  
524 recrystallization, or replacement by calcite. The strength of the new TT proxy, thus,  
525 complements the strengths and compensates for the weaknesses of existing geochemical  
526 methods, especially in shallow marine environments that preserve most of the invertebrate fossil  
527 record. Continuing research on other fossil taxa will enable us to know to what extent the  
528 relationship shown in Figure 7 is taxon-specific, and analyses of shells from controlled modern  
529 growth experiments may allow us to disentangle the effects of metabolism and crystal growth  
530 rate on nacre TT.

531 Finally, the observed T-dependence reveals that the formation of nacre's TT, iridescence,  
532 and fracture toughness (Barthelat et al., 2016) is exquisitely bio-physical in origin, combining  
533 diverse T-dependent parameters, such as bio-metabolic rate and physical crystal growth rate, that  
534 can be harnessed for biomimetic nacre-like materials synthesis (Finnemore et al., 2012; Wegst et  
535 al., 2015).

536

## 537 **5. Acknowledgements**

538 We thank Andreas Scholl and Anthony Young for expert technical help during the experiments.

539 We thank Nami Kitchen, Yunbin Guan and Chi Ma for help with analytical measurements at

540 Caltech. We are indebted to Jessica Cundiff, Susan Butts, Jessica Utrup, Neil Landman, Bushra

541 Hussaini, Robert Hazen, John Nance, Christopher Andrew, and Steven Davies for finding and

542 providing fossil specimens from their museum collections. We thank Jonatahn Erez, Erez  
543 Lieberman-Aiden and Lakshmi Narasimhan for discussions, and C. Kevin Boyce for reading the  
544 manuscript and suggesting improvements. PUPAG acknowledges support from the U.S.  
545 Department of Energy, Office of Science, Office of Basic Energy Sciences, Chemical Sciences,  
546 Geosciences, and Biosciences Division under Award DE-FG02-07ER15899, the Radcliffe  
547 Institute for Advanced Study at Harvard University, NSF grant DMR-1105167, US-Israel  
548 Binational Science Foundation grant BSF-2010065. PEEM and diffraction experiments were  
549 done at the ALS, which is a DOE Office of Science User Facility supported by grant DE-AC02-  
550 05CH11231.  
551 AHK and CEM acknowledge support from the NASA Astrobiology Institute and the NASA  
552 Postdoctoral Program. KDB acknowledges support from the Harvard Society of Fellows.

553  
554 **6. References**  
555

- 556 Alroy, J., Aberhan, M., Bottjer, D.J., Foote, M., Fürsich, F.T., Harries, P.J., Hendy, A.J., Holland,  
557 S.M., Ivany, L.C., Kiessling, W., 2008. Phanerozoic trends in the global diversity of marine  
558 invertebrates. *Science* 321, 97-100.
- 559 Aucoin, S., Himmelman, J., 2011. Factors determining the abundance, distribution and  
560 population size–structure of the penshell *Pinna carnea*. *J Marine Biol Assn UK* 91, 593-606.
- 561 Barthelat, F., Yin, Z., Buehler, M.J., 2016. Structure and mechanics of interfaces in biological  
562 materials. *Nature Reviews Materials*, 16007.
- 563 Be, A.W.H., 1968. Shell porosity of recent planktonic foraminifera as a climatic index. *Science*  
564 161, 881-884.
- 565 Cartwright, J.H., Checa, A.G., 2007. The dynamics of nacre self-assembly. *Journal of the Royal*  
566 *Society Interface* 4, 491-504.
- 567 De Stasio, G., Frazer, B.H., Gilbert, B., Richter, K.L., Valley, J.W., 2003. Compensation of  
568 charging in X-PEEM: a successful test on mineral inclusions in 4.4 Ga old zircon.  
569 *Ultramicroscopy* 98, 57-62.
- 570 Dennis, K.J., Affek, H.P., Passey, B.H., Schrag, D.P., Eiler, J.M., 2011. Defining an absolute  
571 reference frame for ‘clumped’ isotope studies of CO<sub>2</sub>. *Geochim Cosmochim Acta* 75, 7117-7131.
- 572 DeVol, R.T., Metzler, R.A., Kabalah-Amitai, L., Pokroy, B., Politi, Y., Gal, A., Addadi, L.,  
573 Weiner, S., Fernandez-Martinez, A., Demichelis, R., Gale, J.D., Ihli, J., Meldrum, F.C., Blonsky,  
574 A.Z., Killian, C.E., Salling, C.B., Young, A.T., Marcus, M.A., Scholl, A., Doran, A., Jenkins, C.,  
575 Bechtel, H.A., Gilbert, P.U.P.A., 2014. Oxygen spectroscopy and Polarization-dependent

576 Imaging Contrast (PIC)-mapping of calcium carbonate minerals and biominerals. *J Phys Chem B*  
577 118, 8449-8457.

578 DeVol, R.T., Sun, C.-Y., Marcus, M.A., Coppersmith, S.N., Myneni, S.C.B., Gilbert, P.U.P.A.,  
579 2015. Nanoscale Transforming Mineral Phases in Fresh Nacre. *J Am Chem Soc* 137, 13325-  
580 13333.

581 Eiler, J.M., 2007. "Clumped-isotope" geochemistry—The study of naturally-occurring, multiply-  
582 substituted isotopologues. *Earth Plan Sci Lett* 262, 309-327.

583 En-Zhi, M., Boucot, A., Xu, C., Jia-Yu, R., 1986. Correlation of the Silurian rocks of China.  
584 *Geol Soc Amer Special Papers* 202, 1-81.

585 England, J., Cusack, M., Dalbeck, P., Perez-Huerta, A., 2007. Comparison of the  
586 crystallographic structure of semi nacre and nacre by electron backscatter diffraction. *Crystal*  
587 *Growth & Design* 7, 307-310.

588 Finnemore, A., Cunha, P., Shean, T., Vignolini, S., Guldin, S., Oyen, M., Steiner, U., 2012.  
589 Biomimetic layer-by-layer assembly of artificial nacre. *Nature Commun* 3, 966.

590 Frerichs, W.E., Heimann, M.E., Borgman, L.E., Be, A.W.H., 1972. Latitudinal variations in  
591 planktonic foraminiferal test porosity: part 1. optical studies. *J Foram Res* 2, 6-13.

592 GG-Macros, 2016. <http://home.physics.wisc.edu/gilbert/software.htm>.

593 Gilbert, P.U.P.A., 2014. Photoemission spectromicroscopy for the biomineralogist, in: DiMasi,  
594 E., Gower, L.B. (Eds.), *Biom mineralization Sourcebook, Characterization of Biominerals and*  
595 *Biomimetic Materials*. CRC Press, Boca Raton, FL, pp. 135-151.

596 Gilbert, P.U.P.A., Young, A., Coppersmith, S.N., 2011. Measurement of c-axis angular  
597 orientation in calcite (CaCO<sub>3</sub>) nanocrystals using x-ray absorption spectroscopy. *Proc Natl Acad*  
598 *Sci USA* 108, 11350-11355.

599 Gillooly, J.F., Brown, J.H., West, G.B., Savage, V.M., Charnov, E.L., 2001. Effects of size and  
600 temperature on metabolic rate. *Science* 293, 2248-2251.

601 Grave, B.H., 1911. *Anatomy and physiology of the wing-shell Atrina rigida*. Govt. print. off.

602 Henkes, G.A., Passey, B.H., Wanamaker, A.D., Grossman, E.L., Ambrose, W.G., Carroll, M.L.,  
603 2013. Carbonate clumped isotope compositions of modern marine mollusk and brachiopod shells.  
604 *Geochim Cosmochim Acta* 106, 307-325.

605 Huntington, K., Eiler, J., Affek, H., Guo, W., Bonifacie, M., Yeung, L., Thiagarajan, N., Passey,  
606 B., Tripathi, A., Daëron, M., 2009. Methods and limitations of 'clumped' CO<sub>2</sub> isotope ( $\Delta 47$ )  
607 analysis by gas-source isotope ratio mass spectrometry. *J Mass Spectrom* 44, 1318-1329.

608 Jablonski, D., Shubin, N.H., 2015. The future of the fossil record: Paleontology in the 21st  
609 century. *Proc Natl Acad Sci USA* 112, 4852-4858.

610 Kim, J.-H., Schouten, S., Hopmans, E.C., Donner, B., Damsté, J.S.S., 2008. Global sediment  
611 core-top calibration of the TEX 86 paleothermometer in the ocean. *Geochim Cosmochim Acta*  
612 72, 1154-1173.

613 Kim, S.-T., Mucci, A., Taylor, B.E., 2007a. Phosphoric acid fractionation factors for calcite and  
614 aragonite between 25 and 75 C: revisited. *Chem Geol* 246, 135-146.

615 Kim, S.-T., O'Neil, J.R., 1997. Equilibrium and nonequilibrium oxygen isotope effects in  
616 synthetic carbonates. *Geochim Cosmochim Acta* 61, 3461-3475.

617 Kim, S.-T., O'Neil, J.R., Hillaire-Marcel, C., Mucci, A., 2007b. Oxygen isotope fractionation  
618 between synthetic aragonite and water: influence of temperature and Mg<sup>2+</sup> concentration.  
619 *Geochim Cosmochim Acta* 71, 4704-4715.

620 Kozdon, R., Ushikubo, T., Kita, N.T., Spicuzza, M., Valley, J.W., 2009. Intratest oxygen isotope  
621 variability in the planktonic foraminifer *N. pachyderma*: Real vs. apparent vital effects by ion  
622 microprobe. *Chem Geol* 258, 327-337.

623 Lemer, S., Buge, B., Bemis, A., Giribet, G., 2014. First molecular phylogeny of the  
624 circumtropical bivalve family Pinnidae (Mollusca, Bivalvia): evidence for high levels of cryptic  
625 species diversity. *Molec Phylogenet Evol* 75, 11-23.

626 Levi-Kalisman, Y., Falini, G., Addadi, L., Weiner, S., 2001. Structure of the nacreous organic  
627 matrix of a bivalve mollusk shell examined in the hydrated state using cryo-TEM. *J Struct Biol*  
628 135, 8-17.

629 Madix, R., Solomon, J., Stöhr, J., 1988. The orientation of the carbonate anion on Ag (110). *Surf*  
630 *Sci* 197, L253-L259.

631 Metzler, R.A., Abrecht, M., Olabisi, R.M., Ariosa, D., Johnson, C.J., Frazer, B.H., Coppersmith,  
632 S.N., Gilbert, P.U.P.A., 2007. Architecture of columnar nacre, and implications for its formation  
633 mechanism. *Phys. Rev. Lett.* 98, 268102.

634 Metzler, R.A., Zhou, D., Abrecht, M., Chiou, J.-W., Guo, J., Ariosa, D., Coppersmith, S.N.,  
635 Gilbert, P.U.P.A., 2008. Polarization-dependent imaging contrast in abalone shells. *Phys Rev B*  
636 77, 064110-064111/064119.

637 Milano, S., Schöne, B.R., Witbaard, R., 2015. Changes of shell microstructural characteristics of  
638 *Cerastoderma edule* (Bivalvia)—A novel proxy for water temperature. *Palaeogeography,*  
639 *Palaeoclimatology, Palaeoecology.*

640 Olson, I.C., Blonsky, A.Z., Tamura, N., Kunz, M., Gilbert, P.U.P.A., 2013. Crystal nucleation  
641 and near-epitaxial growth in nacre. *J Struct Biol* 184, 454-457.

642 Olson, I.C., Kozdon, R., Valley, J.W., Gilbert, P.U.P.A., 2012. Mollusk shell nacre ultrastructure  
643 correlates with environmental temperature and pressure. *J Am Chem Soc* 134, 7351-7358.

644 Passey, B.H., Levin, N.E., Cerling, T.E., Brown, F.H., Eiler, J.M., 2010. High-temperature  
645 environments of human evolution in East Africa based on bond ordering in paleosol carbonates.  
646 *Proc Natl Acad Sci USA* 107, 11245-11249.

647 Press, W.H., Teukolsky, S.A., Vetterling, W.T., Flannery, B.P., 1996. Numerical recipes in  
648 Fortran 77 and Fortran 90. Cambridge University Press Cambridge.

649 Richardson, C., Peharda, M., Kennedy, H., Kennedy, P., Onofri, V., 2004. Age, growth rate and  
650 season of recruitment of *Pinna nobilis* (L) in the Croatian Adriatic determined from Mg: Ca and  
651 Sr: Ca shell profiles. *J Exper Marine Biol Ecol* 299, 1-16.

652 Rollion-Bard, C., Erez, J., Zilberman, T., 2008. Intra-shell oxygen isotope ratios in the benthic  
653 foraminifera genus *Amphistegina* and the influence of seawater carbonate chemistry and  
654 temperature on this ratio. *Geochim et Cosmochim Acta* 72, 6006-6014.

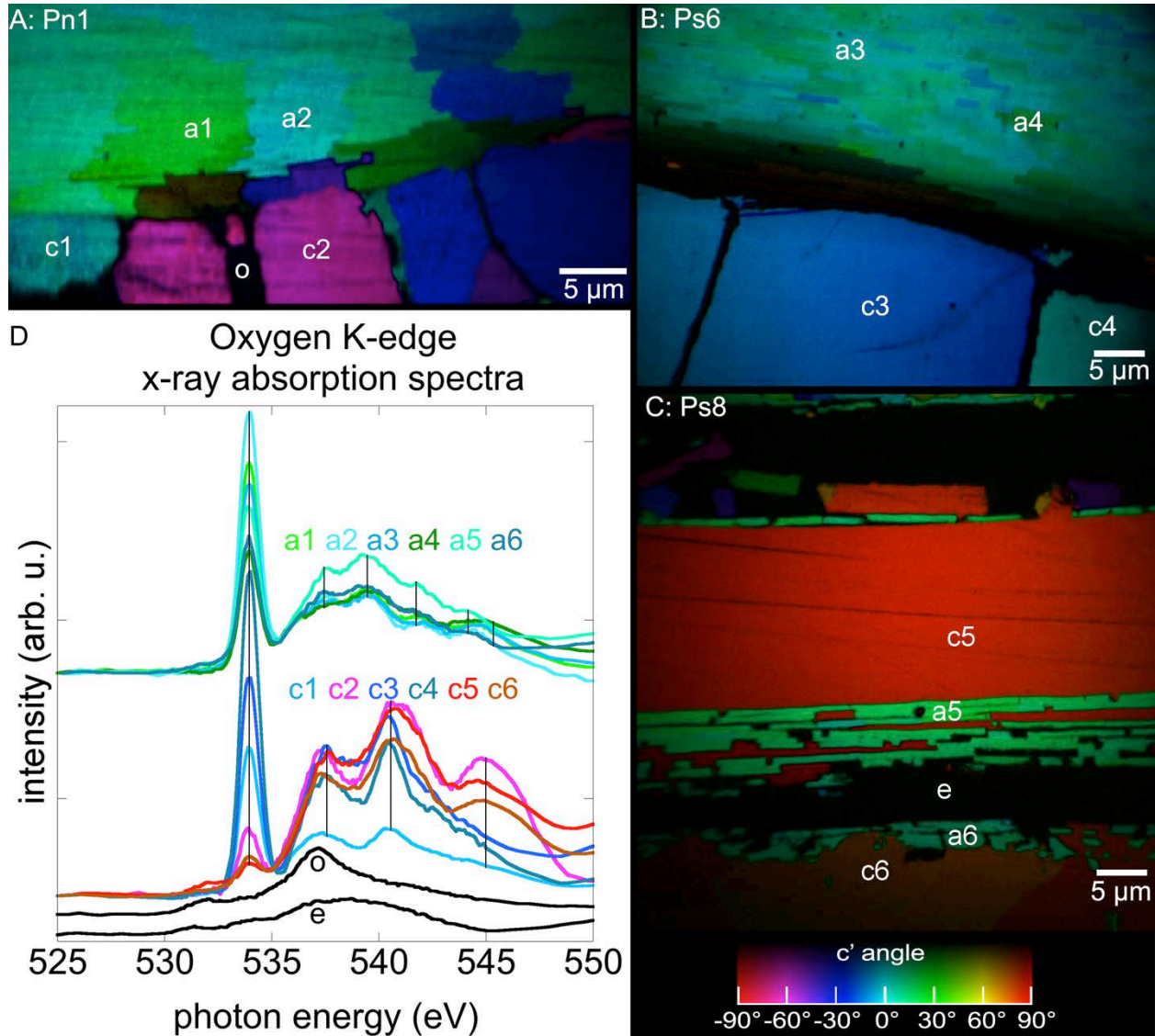
655 Rosales, I., Quesada, S., Robles, S., 2004. Paleotemperature variations of Early Jurassic seawater  
656 recorded in geochemical trends of belemnites from the Basque-Cantabrian basin, northern Spain.  
657 *Palaeogeography, Palaeoclimatology, Palaeoecology* 203, 253-275.

658 Schöne, B.R., Lega, J., Flessa, K.W., Goodwin, D.H., Dettman, D.L., 2002. Reconstructing daily  
659 temperatures from growth rates of the intertidal bivalve mollusk *Chione cortezi* (northern Gulf of  
660 California, Mexico). *Palaeogeography, Palaeoclimatology, Palaeoecology* 184, 131-146.

661 Schultz, P.W., Huber, M., 2013. Revision of the worldwide recent Pinnidae and some remarks on  
662 fossil European Pinnidae. ConchBooks, Öhringen, Germany.

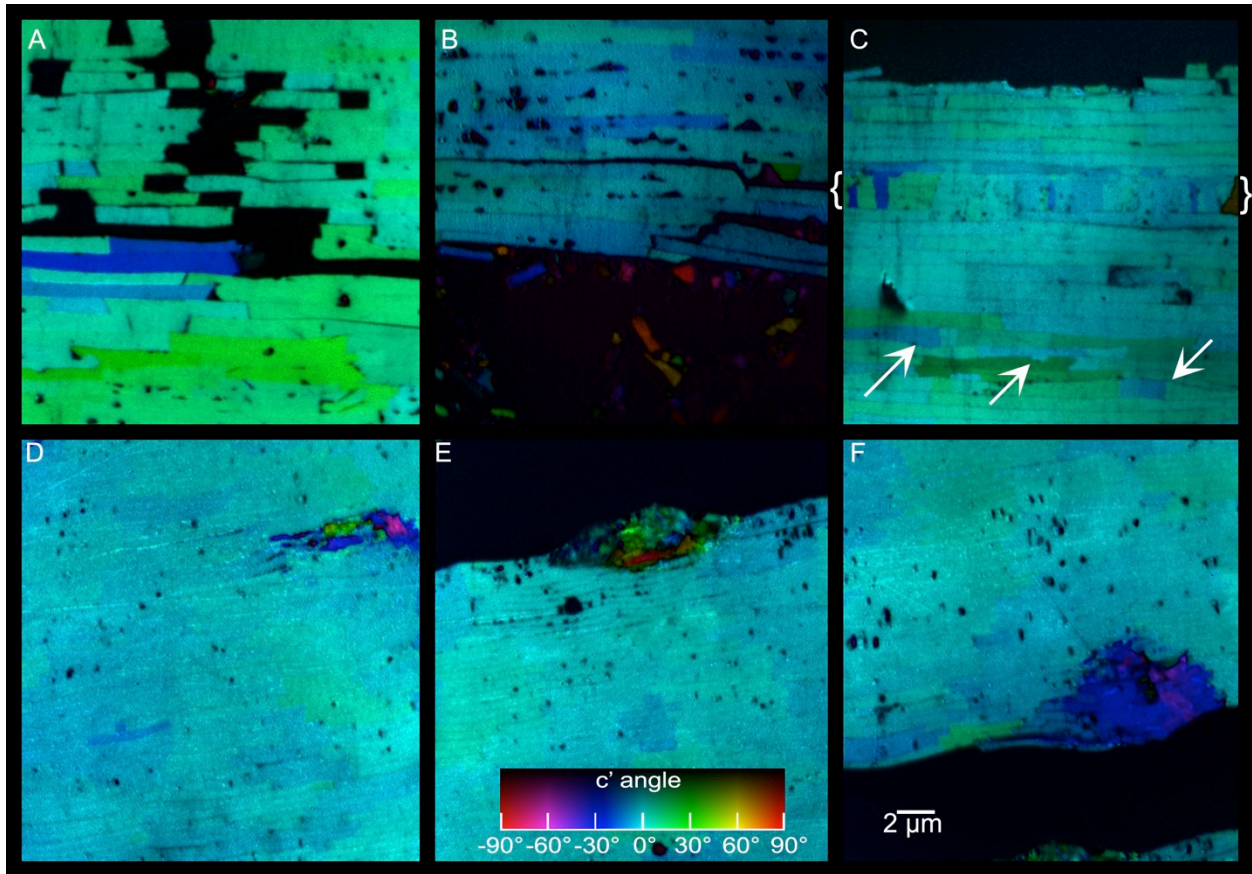
663 Sepkoski Jr, J.J., 1981. A factor analytic description of the Phanerozoic marine fossil record.  
664 *Paleobiol* 7, 36-53.

665 Shtukenberg, A.G., Punin, Y.O., Gunn, E., Kahr, B., 2011. Spherulites. *Chemical reviews* 112,  
666 1805-1838.  
667 Tonner, B.P., Harp, G.R., 1988. Photoelectron microscopy with synchrotron radiation. *Rev Sci*  
668 *Instrum* 59, 853-858.  
669 Turner, R.D., Rosewater, J., 1958. The family Pinnidae in the western Atlantic. *Johnsonia* 3,  
670 285-326.  
671 Wegst, U.G.K., Bai, H., Saiz, E., Tomsia, A.P., Ritchie, R.O., 2015. Bioinspired structural  
672 materials. *Nature Materials* 14, 23-36.  
673 Weiner, S., Lowenstam, H.A., Hood, L., 1976. Characterization of 80-million-year-old mollusk  
674 shell proteins. *Proc Natl Acad Sci USA* 73, 2541-2545.  
675 Wheelton, H., 1905. A monograph of the British Carboniferous Lamellibranchiata Volume II.  
676 Palaeontographical Society.  
677 Zachos, J., Pagani, M., Sloan, L., Thomas, E., Billups, K., 2001. Trends, rhythms, and  
678 aberrations in global climate 65 Ma to present. *Science* 292, 686-693.  
679  
680



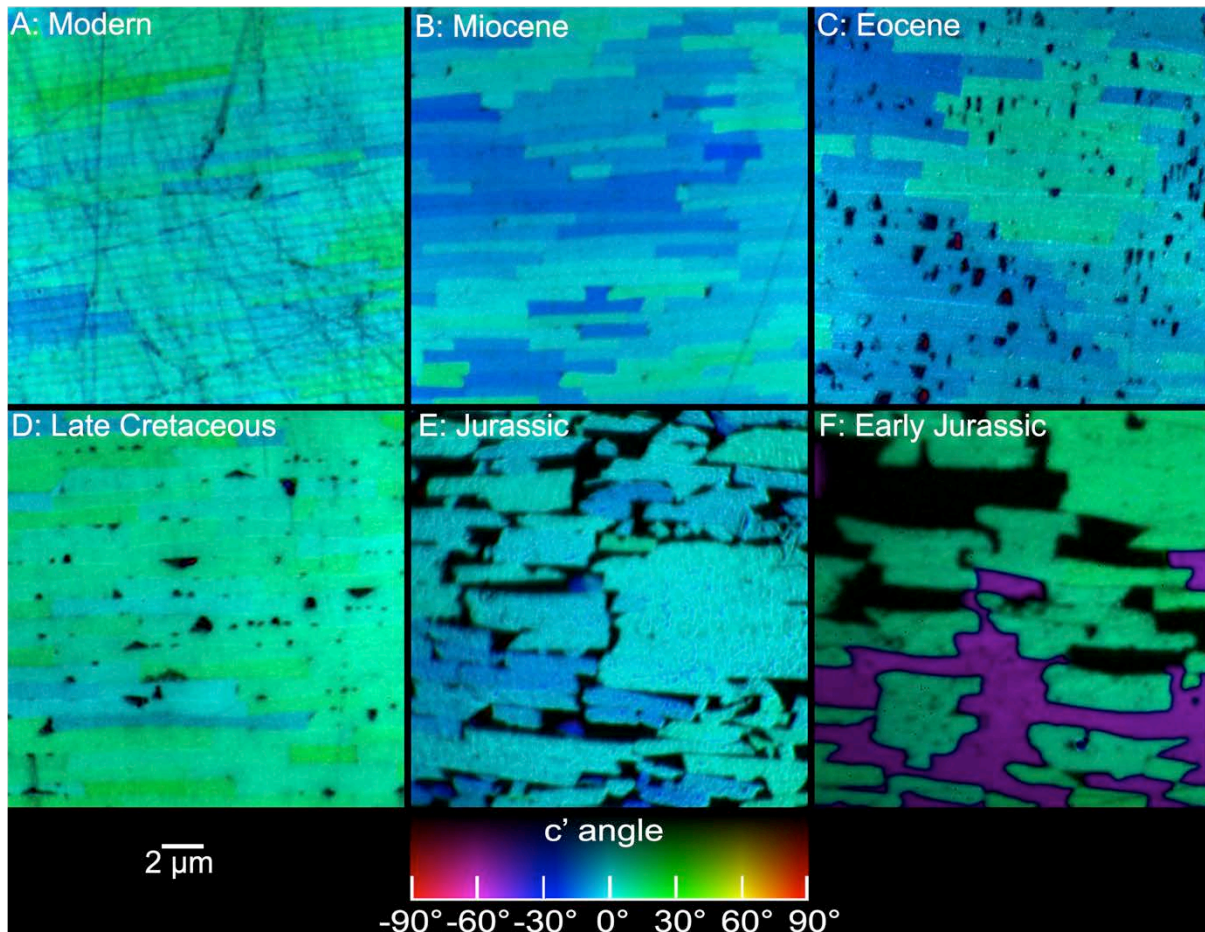
682

683 **Figure 1.** PIC-maps of three *Pinna* shells in cross-section. One **modern** (A: Pn1) and one from the  
 684 Late Cretaceous (B: Ps6) show the excellent preservation of prismatic calcite layer at the bottom  
 685 (c1-4) and aragonite nacre (a1-4) at the top, with dark organic sheets between prisms (o) and  
 686 between prisms and nacre. (C: Ps8) A poorly preserved Jurassic *Pinna* shell: dissolved and re-  
 687 crystallized regions show mis-oriented calcite (c5-6) interspersed with intact aragonite nacre (a5-  
 688 6), and holes filled with epoxy (e). Colors identify different c-axis crystal orientations (color legend  
 689 at bottom right). (D) Oxygen spectra extracted from  $\sim 2\mu\text{m}$  squares correspondingly labeled and  
 690 colored regions in all PIC-maps. Aragonite and calcite have 6 and 4 peaks, respectively (vertical  
 691 lines). Peak amplitudes differ for differently oriented crystals, generating the colors in PIC-maps.



692  
 693 **Figure 2.** The effect of diagenesis on fossil nacre. (A) sample Ps5-1 (Late Cretaceous)  
 694 showing a crack (black) propagating through nacre. Notice that the blue and green tablets  
 695 are 60° apart in crystallographic orientation. This is unusual in nacre, where the angle  
 696 spread in a single image of intact nacre is always 30° or less (Metzler et al., 2008; Olson et  
 697 al., 2013; Olson et al., 2012). Despite minor re-crystallization at off-angles, overall tablet  
 698 morphology is preserved. This recrystallization was observed only twice in 858 PIC-maps.  
 699 (B) Ps6-1 (Late Cretaceous) showing broken nacre near a gap (bottom, black), in which  
 700 displaced tablets have different orientations (off-colors), as expected due to breakage.  
 701 Tablets still in place have the usual colors near cyan. This is the most frequent difference  
 702 observed between modern and fossil shells. (c) Ps6-1 (Late Cretaceous) near a gap (top,  
 703 black). Three nacre tablet layers (between curly brackets) appear to have dissolved and re-  
 704 precipitated with altered morphology. This is the only observation of this phenomenon in  
 705 this or any other nacre sample. The orientation is off at the extreme left and right, but usual  
 706 at the center, likely because re-crystallization occurred by epitaxial growth on nacre tablets.  
 707 Other tablets (arrows) have altered morphology. (D,E,F) Px1-1 (Early Eocene) showing

708 three regions with dramatically altered morphology and crystal orientations, likely the  
709 result of re-crystallization. Surprisingly, the polymorph in the re-crystallized regions is  
710 aragonite, as demonstrated by oxygen spectra, similar to those in **Figure 3**. These re-  
711 crystallized areas in (D,E,F) are the only three cases, in 822 areas analyzed in **Modern**-  
712 Cretaceous shells, of such dramatic morphology and orientation changes.  
713



714  
715 **Figure 3.** Nacre PIC-maps from the five geologic epochs in this study. Colors identify  
716 different c-axis crystal orientations (see color legend) and differentiate individual nacre  
717 tablets, even in the presence of surface scratches (A) or missing fragments of nacre tablets  
718 (black in C,D,E,F). Despite the disruption in structure in E, the crystal orientations are intact  
719 with a nearly vertical c-axis (cyan and neighboring turquoise colors, thus  $\pm 15^\circ$ ). Even in F  
720 some nacre tablets show no diagenesis, even in immediate contact with holes (black), or  
721 diagenetic, recrystallized calcite (purple).

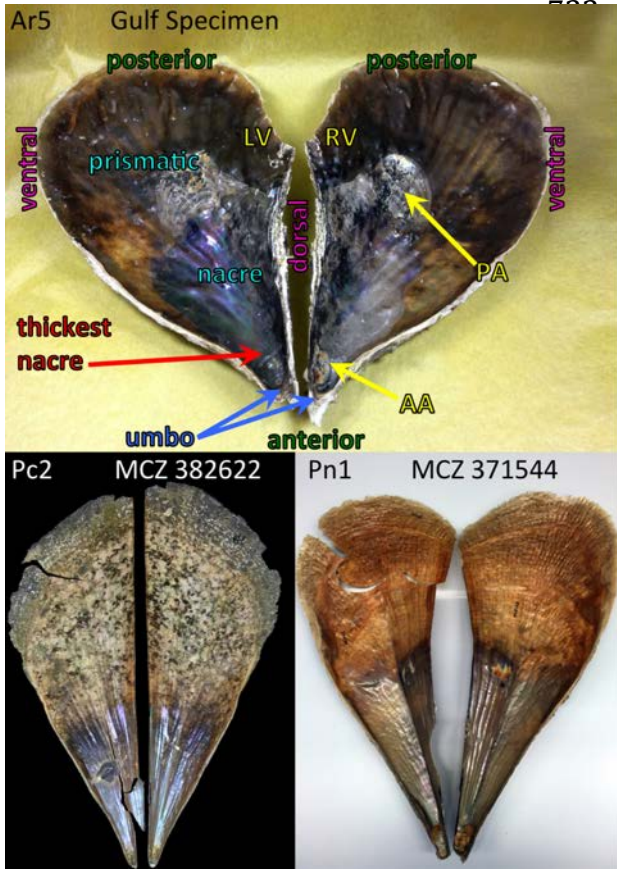
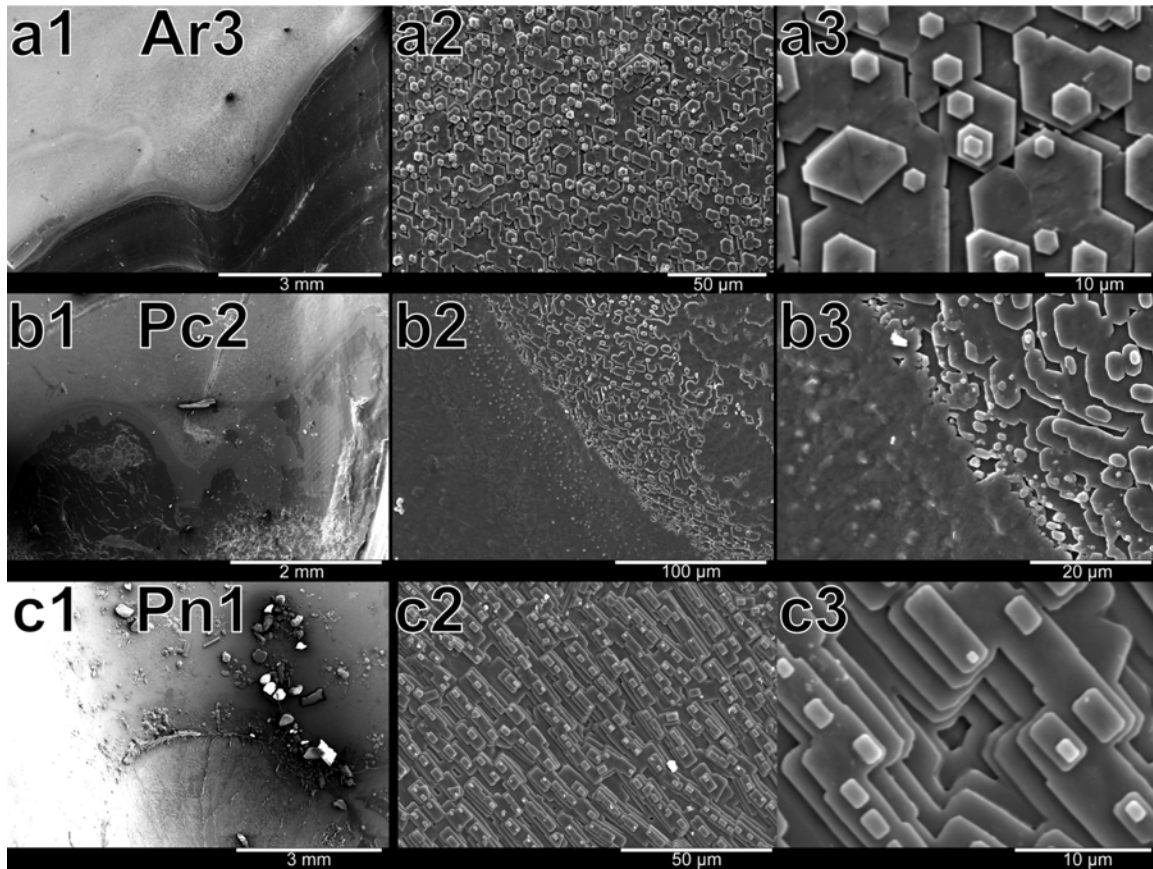


Figure 4. Photographs of the 3 modern shells analyzed here: *Atrina rigida* (shell Ar5), *Pinna carnea* (shell Pc2), and *P. nobilis* (shell Pn1). Modern specimens are nearly complete and illustrate relevant anatomy for analysis, as labeled on specimen Ar5. In the photo, the hinge is shown as vertical and separates the left and right valves (LV and RV respectively). In Pinnidae, nacre covers  $\frac{1}{2}$  to  $\frac{3}{4}$  of the total shell area in each valve. Note in Ar5 that the posterior adductor muscle scars (PA) are visible protruding posterior to the nacreous region in *Atrina* specimens. PAs are fully enclosed within the nacre in species of *Pinna*, e.g. Pc2 and Pn1 shown here. *Pinna* may also be distinguished by a sulcus (groove)

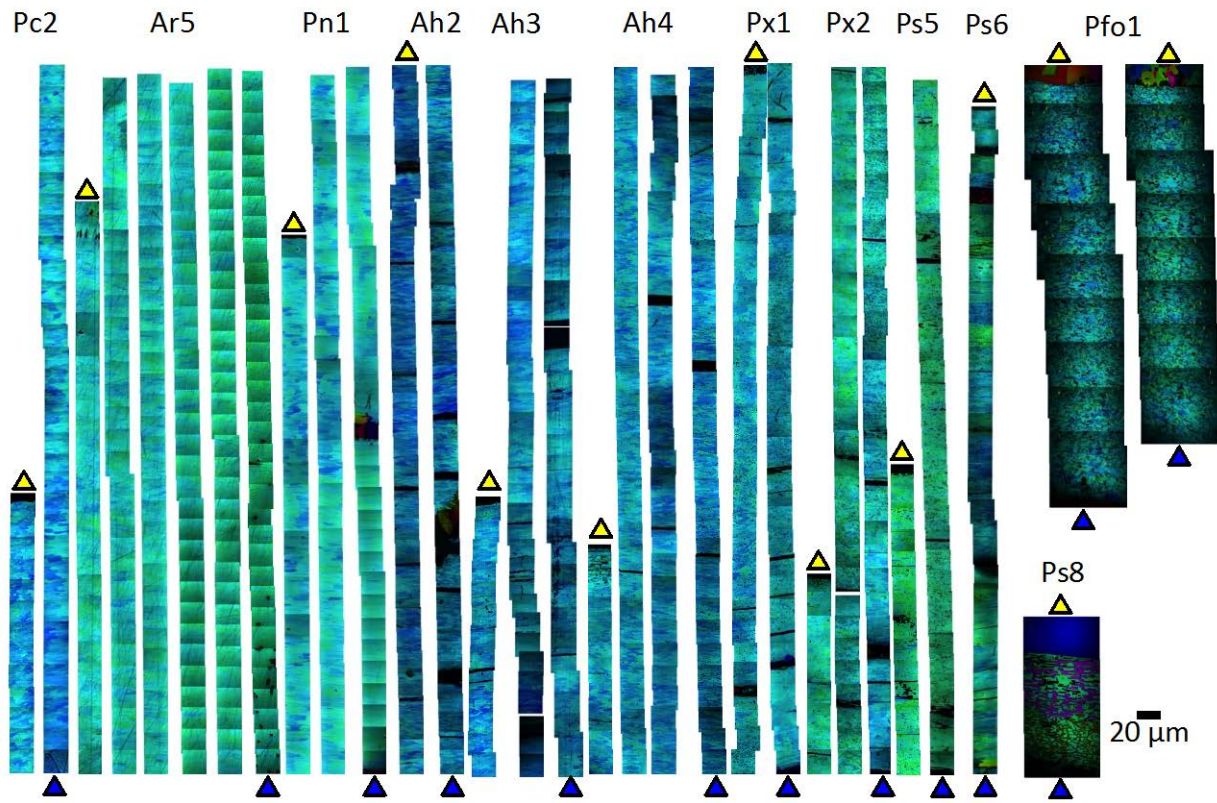
738 separating the nacreous region into two lobes, which is absent in species of *Atrina*. The  
 739 anterior regions of both genera, however, are identical at all scales (i.e., from naked eye to  
 740 SEM). This includes the umbo, the anterior adductor muscle scars (AA), prismatic calcite,  
 741 and aragonite nacre. Importantly, the relative position of the thickest nacre is the same in  
 742 specimens from both genera, and easily identifiable as a slightly bulging surface  $\sim 2$  mm  
 743 posterior to the AAs (shown at higher magnification in Figure 5). This region is well  
 744 preserved in fossils, as shown in Figure S5.

745  
 746  
 747  
 748  
 749  
 750



751  
 752 **Figure 5.** SEM micrographs of the surface of the region of thickest nacre in three modern  
 753 shells: Ar3, Pc2, Pn1. The anterior adductor muscle scars (AAs) are visible at the bottom of  
 754 **a1, b1, c1**, the thickest part of nacre is ~2 mm posterior of the AAs, at the center of **a1, b1,**  
 755 **c1**. The magnification increases to the right; Panels 2 and 3 illustrate the same region of  
 756 thickest nacre, which is the location of cross-sections for PEEM analysis. Panels **a3, b3, c3**  
 757 demonstrate that nacre is still forming in this thickest part of nacre, at the time of the  
 758 mollusk's death.

759  
 760



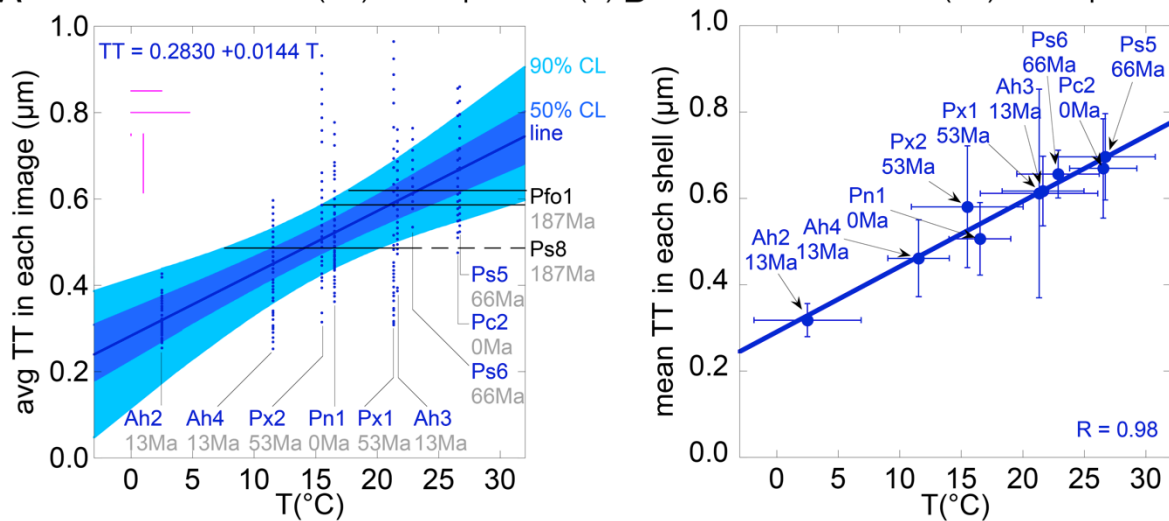
▲ = interior of shell, last deposited    ▲ = exterior of shell, first deposited

761  
 762 **Figure 6.** The series of PIC-maps (842 in total) produced from the twelve specimens  
 763 analyzed in this study, and described in **Table S1**. In each vertical series, partly-overlapping  
 764 PIC-maps capture naacre ultrastructure uninterrupted through the full cross-section of the  
 765 shell. The bottom right (blue triangle) of each PIC-map series shows the oldest naacre, which  
 766 was deposited first and in contact with the prismatic layer when the shell was formed; the  
 767 top left (yellow triangle) shows the youngest naacre, which was deposited most recently,  
 768 and in contact with the mantle cavity in the living animal. Note that in some specimens the  
 769 oldest naacre layer may currently act as the exterior of the shell if the prismatic layer was  
 770 not preserved (see **Figure S5**). In a living individual, the prismatic and nacreous layers are  
 771 attached by an organic layer, which can be preserved even in Late Cretaceous shells (**Figure**  
 772 **1**). Ar5-1 has the thickest nacre layer (~3200 μm), hence six PIC-map series are needed to  
 773 illustrate its cross section. The thinnest specimens are Ps6-1, with only a single series  
 774 (~600 μm), Pfo1-3 with two series, acquired parallel to one another approximately 900 μm

775 apart, in the thickest nacre layer remaining, which was only ~300 μm thick, and Ps8-2, with  
 776 only 90 μm-thick nacre, partly recrystallized (purple calcite) nacre.

777

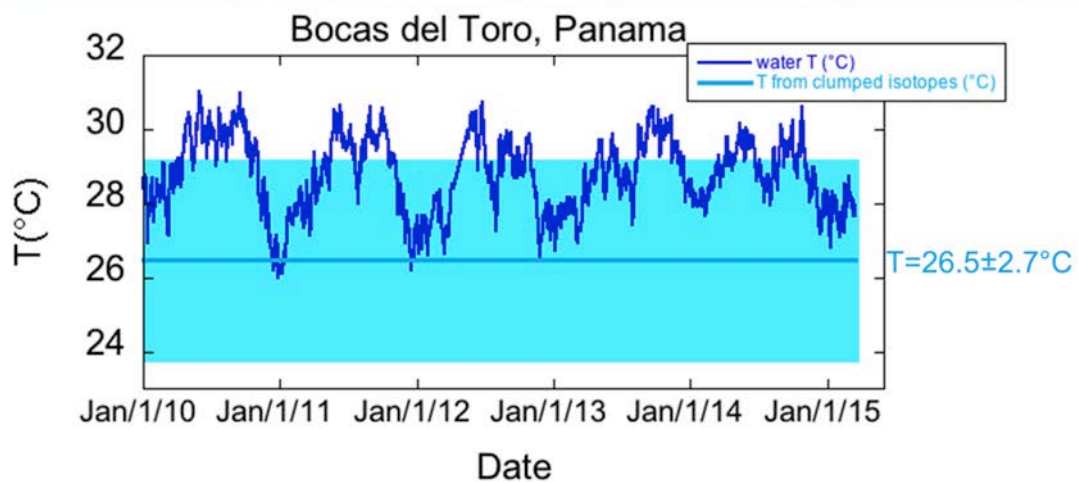
A nacre tablet thickness (TT) vs temperature (T) B nacre tablet thickness (TT) vs temperature (T)



778

779 **Figure 7A.** Nacre tablet thickness (TT) of modern and fossil shells is correlated with  
 780 formation temperature (T). All TTs in each shell cross-section are measured  
 781 microscopically from each of 630 PIC-maps, as shown in **Figures 6, S9, S10**. T was  
 782 independently measured with carbonate clumped isotope analysis from a shell fragment  
 783 adjacent to the PIC-mapped area. The blue “line” is the most probable estimate fit,  $TT (\mu\text{m})$   
 784  $= 0.2830 + 0.0144 T (\text{°C})$ , obtained from 100,000 linear fits, each taking into account all  
 785 errors. The darker and lighter blue shaded areas indicate the 50% and 90% confidence  
 786 level (CL) intervals, respectively. The minimum and maximum error bars are shown in  
 787 magenta on top left for clarity. These are St Dev for TT and St Error of the Mean for T.

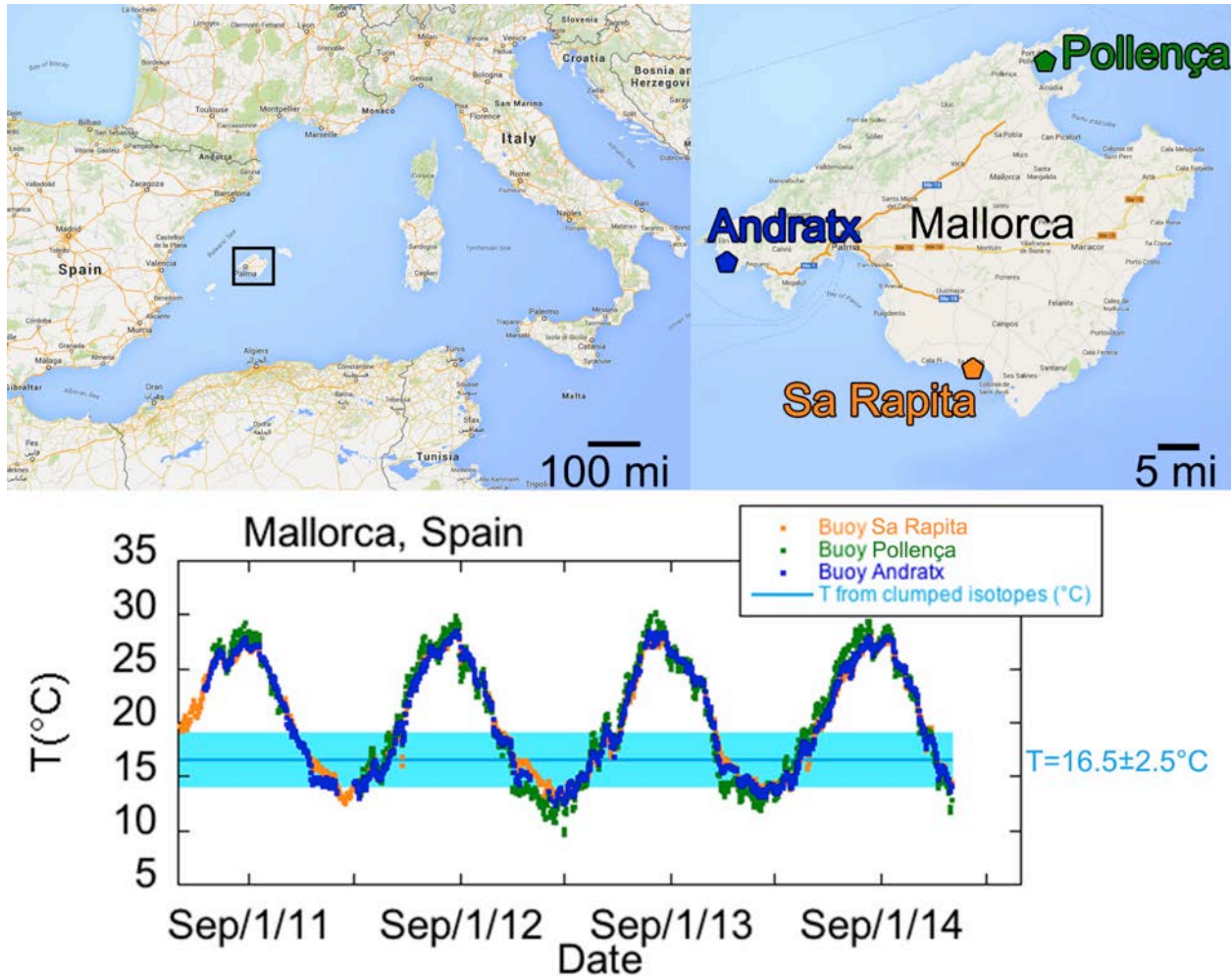
788 **Figure 7B.** Mean nacre tablet thickness (TT) correlates with temperature (T). All TTs in  
 789 are measured microscopically from each of 630 PIC-maps, then averaged for each of the 9  
 790 shells. As in **Figure 7A**, T was measured with clumped isotopes. All error bars are shown.  
 791 These are St Dev for TT and St Error of the Mean for T. The error bars are *not* taken into  
 792 account in the linear fit of 9 points. All data for this figure are provided in **Table S4**.



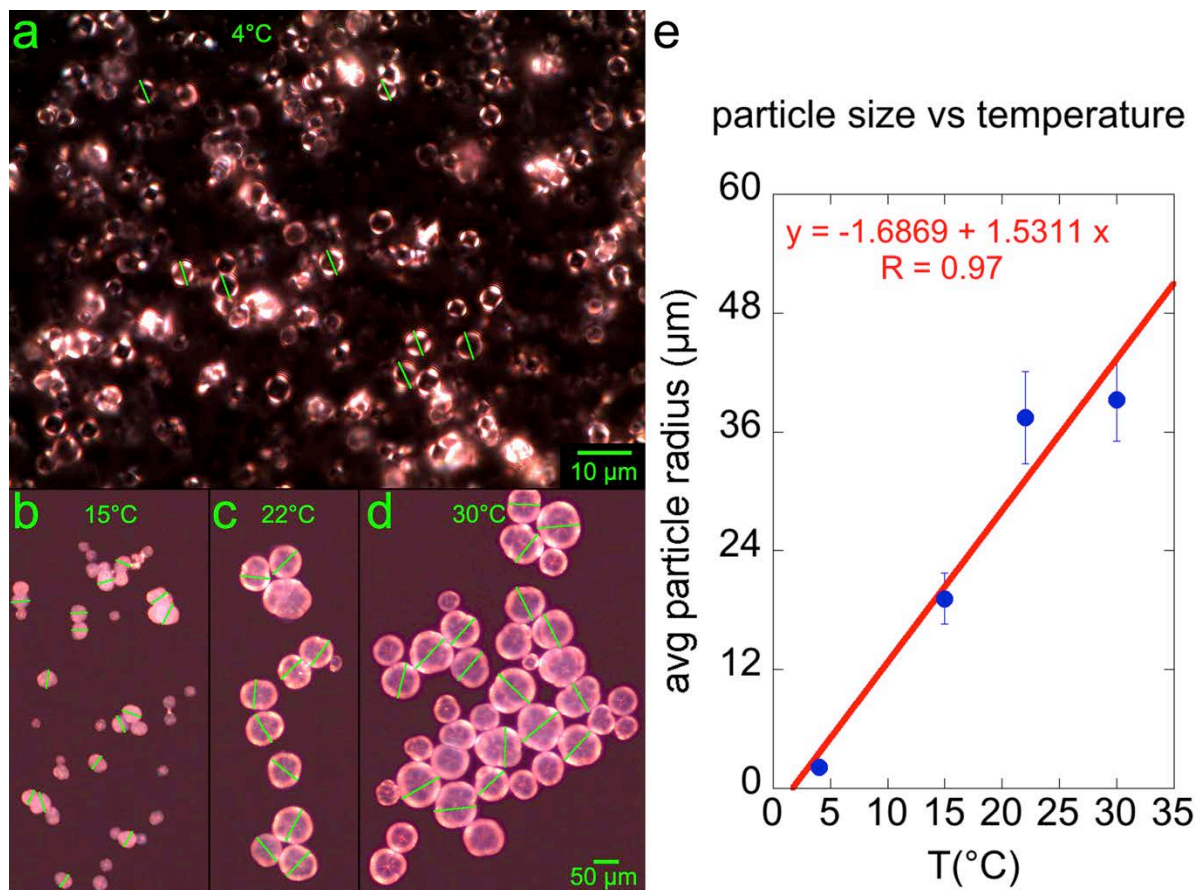
793  
 794 **Figure 8.** Location of Pc2 shell collection (red pentagon S) in Bocas del Toro, Panama, and  
 795 the “Tower” marine weather station (blue pentagon T), where water temperature was  
 796 measured. The shell was collected in a seagrass bed in Boca del Drago, on the NW side of  
 797 Isla Colon, at coordinates 9.40498 N, 82.32411 W. The Tower station is located at 9°21’02”  
 798 N, 82°15’28” W, which is SW of the same island, less than 4 miles away from the shell  
 799 collection site. In this figures, as well as in **Figures 9 and S11**, the box on the left map  
 800 indicates the magnified region on the right. At the bottom are T data from the weather  
 801 station (dark blue oscillating line) and clumped isotope analysis of the shell. The weather  
 802 station temperature and other data are further described  
 803 at : [http://biogeodb.stri.si.edu/physical\\_monitoring/research/bocas](http://biogeodb.stri.si.edu/physical_monitoring/research/bocas) . Notice the  
 804 agreement of the clumped isotope-measured temperature (light horizontal blue line in the  
 805 plot) and its error range (cyan shaded area) in the shell, and the temperature recorded by a

806 thermometer in the water. From these data we deduce that the region of Pc2 shell analyzed  
 807 by both clumped isotopes (T) and PEEM (TT) was formed in less than one year, and mostly  
 808 during the colder months.

809



810  
 811 **Figure 9.** Approximate location of Pn1 shell collection in waters surrounding Mallorca,  
 812 Spain. Three marine weather buoys used for T data are also shown (colored pentagons)  
 813 and described  
 814 on: <http://www.socib.es/index.php?seccion=observingFacilities&facility=mooring>. Notice  
 815 the agreement of the temperature and its error range (cyan shaded area in the plot), as  
 816 measured by the clumped isotope thermometer in the shell, and the temperature recorded  
 817 by thermometers in the water. From these data we deduce that the region of Pn1 analyzed  
 818 was formed in less than one year, and mostly during the colder months.



819  
 820 **Figure 10.** Aragonite growth *in vitro*. Visible light microscopy (VLM) with crossed  
 821 polarizers. Aragonite particles grow spherulitically, i.e, with a radial distribution of acicular  
 822 crystals, each with the c-axis along the radius of the sphere (Shtukenberg et al., 2011). In  
 823 cross-polarized light, therefore, all crystals along a cross are extinguished, and the  
 824 remainder form a bright and unique “Maltese cross” pattern. Four sets of synthetic  
 825 aragonite particles were allowed to grow from solution at different temperatures: 4°C, 15°C,  
 826 22°C, and 30°C. Note that this is in the absence of any organic molecules. For the lowest  
 827 temperature several different kinds of particles were observed, but we selected only the  
 828 ones with a visible Maltese cross, confirming the presence of aragonite. For higher  
 829 temperatures (15°, 22°, 30°C) only spherulitic particles were observed. Particle diameters  
 830 were measured in 100 particles per T treatment, these were averaged, then divided by 2 to  
 831 display the average radius in the plot of size vs T. A clear trend of increasing particle size  
 832 with increasing temperature is visible.

833

## Supporting information

for

### Nacre tablet thickness records formation temperature

### in recent and fossil shells

Pupa U.P.A Gilbert<sup>1,2\*</sup>, Kristin D. Bergmann<sup>3,4</sup>, Corinne E. Myers<sup>5,6</sup>, Matthew A. Marcus<sup>7</sup>, Ross T. DeVol<sup>1</sup>, Chang-Yu Sun<sup>1</sup>, Adam Z. Blonsky<sup>1</sup>, Erik Tamre<sup>2,3</sup>, Jessica Zhao<sup>2</sup>, Elizabeth A. Karan<sup>2</sup>, Nobumichi Tamura<sup>7</sup>, Sarah Lemer<sup>5</sup>, Anthony J. Giuffre<sup>1</sup>, Gonzalo Giribet<sup>5</sup>, John M. Eiler<sup>8</sup>, Andrew H. Knoll<sup>3,5</sup>

<sup>1</sup> University of Wisconsin–Madison, Departments of Physics, Chemistry, Geoscience, Madison WI 53706 USA.

<sup>2</sup> Harvard University, Radcliffe Institute for Advanced Study, Fellowship Program, Cambridge, MA 02138.

<sup>3</sup> Harvard University, Department of Earth and Planetary Sciences, Cambridge, MA 02138.

<sup>4</sup> Massachusetts Institute of Technology, Department of Earth, Atmospheric and Planetary Sciences, Cambridge, MA 02139.

<sup>5</sup> Harvard University, Museum of Comparative Zoology and Department of Organismic and Evolutionary Biology, Cambridge, MA 02138.

<sup>6</sup> University of New Mexico, Department of Earth and Planetary Sciences, Albuquerque, NM 87131.

<sup>7</sup> Advanced Light Source, Lawrence Berkeley National Laboratory, Berkeley, CA, 94720, USA.

<sup>8</sup> California Institute of Technology, Division of Geological and Planetary Sciences, Pasadena, CA 91125

\* corresponding author, pupa@physics.wisc.edu, previously publishing as Gelsomina De

Stasio

### **Pinnidae: an ideal family for this study**

Specimens within the family Pinnidae, commonly called pen shells or pen clams, were chosen for this study for several reasons. Pinnids are not uncommon in both the modern and fossil records (Figure S1). Thus, modern specimens enabled ground-truthing of the nacre TT-based paleothermometer, and fossil specimens provided a unique window into paleoclimate over 180 Ma of Earth history. Pen shells are large, fast growing bivalves with a thick nacreous region ideal for both spectral and isotopic analyses. Furthermore, the nacre layer in pinnids is easily separated from the prismatic calcite layer. This facilitates sample preparation and minimizes contamination of aragonite nacre with calcite prisms for clumped isotope analysis. Finally, pinnids produce each shell transect in a relatively short period of time, less than a year. Thus comparison with recent shells, grown at known T, makes it possible to identify which shells were primarily deposited in cooler vs. warmer seasons. Anecdote has it that Japanese pearl farmers harvest their pearls in winter, as the tablet thickness is lower, resulting in greater pearl luster (Strack, 2001). This trend in the Japanese pearl bivalve *Pinctada fucata* is similar to that observed in this work for Pinnidae: greater TT at higher T and *vice versa*.

Seven fossil specimens were analyzed for both TT and T, drawn from three locations reflecting warm geologic times and places (the Late Cretaceous Gulf Coastal Plain, ~ 65.5-66 Ma (Landman et al., 2004; Larina, 2015; Thibault and Gardin, 2006, 2007); the Early Eocene Gulf Coastal Plain, ~ 52-54 Ma (Agnini et al., 2007; Frederiksen et al., 1982; Sessa et al., 2012); and the Middle Miocene Mid-Atlantic Calvert Cliffs, ~ 12.7-13.2 Ma) (Kidwell, 1997). In addition, two Jurassic *Pinna* shells were analyzed for TT only, and T was deduced from TT. Many more details are provided in the Pinnidae biology section below.

### **Pinnidae Biology**

The family Pinnidae Leach, 1819 includes subtidal and coastal species (Dance, 2013) found in tropical and temperate regions, both today and in the fossil record. Pinnid species are important elements of certain marine ecosystems, including the sandy substrate of seagrass beds, lagoons and coral reefs where they can sometimes aggregate in large densities (Rosewater, 1961). Pinnids are sessile, suspension-feeding bivalves found partially buried with their anterior end in sand or mud, such that only the posterior prismatic portion of the shell is visible above the sediment (Aucoin and Himmelman, 2011b; Schultz and Huber, 2013; Turner and Rosewater, 1958; Yonge, 1953b). The family contains two extant genera and 55 accepted species (although there are more than 16 additional genera in the fossil record) (Lemer et al., 2014; Rosewater, 1961; Schultz and Huber, 2013; Turner and Rosewater, 1958). Pinnids are united by an elongated subtrigonal shell shape, heteromyarian adductor muscle scars (small in the anterior and large in the posterior), a toothless hinge with primary and secondary ligament segments, thin to absent periostracum, byssus, and generally large size (commonly between 15-35cm; Recent *Pinna nobilis* may reach lengths over 1m (Richardson et al., 2004a; Schultz and Huber, 2013; Turner and Rosewater, 1958)). Pinnidae is nested within the Order Pterioidea in Pteriomorpha. However the exact position of Pinnidae and the identity of its sister group remains unclear. Earlier studies based on molecular data have suggested a sister group relationship to Pterioidea, Ostreoidea, or Mytiloidea (Adamkewicz et al., 1997; Bieler et al., 2014; Campbell, 2000; Giribet and Distel, 2003; Giribet and Wheeler, 2002; Matsumoto, 2003; Steiner and Hammer, 2000).

The biomineralized shells of the Pinnidae are composed of an outer calcitic prismatic layer and an inner aragonitic nacreous layer. In pen shells the inner nacreous region does not extend to the posterior margin of the prismatic outer shell, and instead extends from the anterior margin approximately 1/3 to 2/3 the length of the shell (Figure 4). The genera *Pinna* Linnaeus, 1758 and *Atrina* Gray, 1842 may be distinguished by the shape and size of their nacreous layer. In species of the genus *Pinna* the internal nacreous layer is divided by a sulcus into a dorsal and a ventral lobe. The position of the posterior adductor muscle scar with respect to the margins of the nacreous layer is one of the major taxonomic characters used to distinguish species. The posterior adductor muscle scars (PAs in Figure 4) in *Pinna* are fully enclosed within the nacreous region (in the dorsal lobe), whereas in *Atrina* PAs extend to the edge of the nacreous layer, and in some species even beyond the margin into the prismatic portion of the shell (Rosewater, 1982; Schultz and Huber, 2013; Turner and Rosewater, 1958; Yonge, 1953b). Finally, in species of the subgenus *Streptopinna* Martens, 1880 (considered a third extant genus until Lemer et al. 2014 (Lemer et al., 2014)) the internal nacreous layer is reduced to a dorsal lobe. The present work focused on species within the extant genera *Atrina* and *Pinna*. These two genera are common in the fossil record and thus provide the most robust history of environmental conditions through time.

Very little is known about the reproductive strategies and the pelagic larval duration of most pinnid species, except for some commercially important ones. Most species are believed to be gonochoristic, to reproduce annually and to produce larvae with a planktotrophic stage with trochophore and veliger stages like *Pinna atropurpurea*, *Atrina pectinata* and *Atrina maura* (Beer and Southgate, 2006; Mendo et al., 2011). Because of their potentially long larval pelagic phase, the dispersal capacity of pinnids is expected to be extensive. This results in a cosmopolitan generic and family distribution, while habitat specificity and past geographic isolation maintained a degree of species-level endemism (e.g. *P. nobilis* in the Mediterranean Sea). Once the veliger settles, the muscular foot is used to bury in soft sediments. Anterior byssus threads then anchor the shell to hard substrate or cobbles in the sediment, such as sea grass beds or coral boulders (Aucoin and Himmelman, 2011a, b; Grave, 1911; Richardson et al., 2004b, a; Rosewater, 1982; Schultz and Huber, 2013; Turner and Rosewater, 1958; Yonge, 1953a, b). Consequently, most species of Pinnidae live within the subtidal photic zone (up to ~ 100 m) (Grave, 1911; Richardson et al., 1999; Schultz and Huber, 2013). Some exceptions exist, e.g., *P. carnea* and other species found in the Pacific Ocean can be found intertidally, and a few species are only found in deep water, down to 600m depth (Schultz and Huber, 2013; Yonge, 1953b). Pen shells are fairly delicate, and may be damaged by wave action, currents, storms, or predation (Allen, 2011; Aucoin and Himmelman, 2011b; Grave, 1911; Rosewater, 1982; Turner and Rosewater, 1958; Yonge, 1953b). Repair of the prismatic portion of the shell is quite efficient. For instance recent *A. rigida* may repair up to 13mm/day (Grave, 1911), and fully exhumed shells may re-bury themselves. However, successful re-burial is not guaranteed, and exhumation often results in death (Grave, 1911; Richardson et al., 1999; Yonge, 1953b).

*Growth Rates.*—Species of pen shells are some of the fastest growing bivalves known and may grow upwards of 20cm or more radially in their first year of life (Aucoin and Himmelman, 2011b; Butler and Brewster, 1979; Cendejas et al., 1985; Richardson et al., 1999; Richardson et al., 2004a). As in most mollusks, faster radial growth occurs early in life; for pen shells this is generally in the first three years (Butler and Brewster, 1979; Schöne, 2008). Individuals reach reproductive maturity in approximately the second year, and have been known to live up to 20 years in the wild (Aucoin and Himmelman, 2011b; Hendriks et al., 2012; Kožul et al., 2011; Richardson et al., 1999).

Slowdown and even stoppage in radial growth with age has been observed in many mollusk species (e.g. (Schöne, 2008); for species of *Pinna* (Grave, 1911; Hendriks et al., 2012)). Furthermore, both biotic and abiotic environmental factors appear to influence rates of shell growth and stoppages. In addition to age, biotic factors affecting mollusk radial growth rates include: availability of nutrients (food), predation pressure, production of gametes, and spawning (Grave, 1911; Ivany, 2012; Joubert et al., 2014; Linard et al., 2011; Lowenstam and Weiner, 1989; Schöne, 2008). Abiotic factors include: temperature, salinity, lunar cycles and tides, seasonal variations (e.g., day length, storms), turbidity, ocean circulation patterns, sea level, and carbon (organic and inorganic), phosphate, and nitrate concentrations in the water column (Ivany, 2012; Joubert et al., 2014; Linard et al., 2011; Lowenstam and Weiner, 1989; Richardson et al., 1999; Schöne, 2008). Changes in growth rates are commonly detected in bivalves by the deposition of a growth line in the prismatic outer shell (Schöne, 2008). These growth lines, unfortunately, are not produced in species of Pinnidae; however, the posterior adductor muscle scars (PAs in Figure 4) can be used to identify the age of individuals (Butler and Brewster, 1979; Richardson et al., 1999; Richardson et al., 2004a). Richardson et al. (Richardson et al., 1999) have documented that PAs from the first year of growth are often absent, thus the age of an individual may be estimated as 1 + number of observed PAs.

Few previous studies have measured slowdowns or stoppages specifically in rates of deposition of the nacreous layer, and none of these were conducted on pen shells. We do not observe any discontinuity in nacre formation for the specimens of *Pinna* and *Atrina* analyzed here (Figure 6), however this does not preclude faster growth seasonally. The most commonly investigated species are those of economic value in pearl aquaculture or human consumption, such as the pearl oyster (*Pinctada margaritifera*) or abalone (e.g., *Haliotis refuscens*). In these few studies, both temperature and nutrient concentrations were observed to impact rates of nacre deposition and total nacre thickness in tank experiments of *P. margaritifera* (Joubert et al., 2014; Linard et al., 2011). Additionally, different suites of genes have been identified in *P. margaritifera* that produce different regulatory proteins for prismatic (radial) vs. nacreous growth (Joubert et al., 2014; Marie et al., 2012). It is very plausible that pen shells, which are closely related to the pearl oysters, share this same genetic framework. Thus, rate of nacre deposition and TT in pen shells may be influenced by abiotic and biotic environmental factors differently than prismatic radial growth, or even continue at a regular rate throughout the life of these species, as the shells of Pinnidae and *Pinctada* thicken significantly after the phase of rapid radial growth (~3 years).

*Fossil Record.*—The Pinnidae are observed in the fossil record as far back as the Silurian Period (~ 444 Ma) (En-Zhi et al., 1986; Zhang, 1988). A PaleoBiology DataBase

(PBDB; [paleobiodb.org/](http://paleobiodb.org/)) search on 5/25/15 recovered 926 fossil occurrences of *Pinna* and 176 fossil occurrences of *Atrina*, with global distribution (see maps from time periods of interest in [Figure S1](#)). *Pinna* first occurs in Middle Mississippian sediments (age range: 345 Ma – present) ([Cash, 1882](#); [Wheelton, 1905](#)); *Atrina* is also first observed in the Carboniferous (age range: ~ 359 Ma – present) ([Rosewater, 1961](#); [Ruedemann, 1916, 1918](#)). Although their delicate shells result in difficulty preserving whole body fossils, fragments and partial specimens are not uncommon in warm water, near-shore to offshore paleo-sediments, where their unique morphology makes for easy identification. Further, when preserved in situ, individuals of Pinnidae are often quite abundant in “thickets”, akin to recent Mytilidae ([Butler and Brewster, 1979](#); [Idris et al., 2008](#)).

## DETAILED METHODS

### Sample acquisition

We apply a specimen naming convention where the first letter designates the genus, second letter designates the species, and the number indicates the order in which the specimen was received and analyzed. Each sample is further identified by a hyphen and either a “1” (fragment analyzed using PEEM) or “2” (fragment analyzed using clumped isotopes), or greater numbers for additional samples. For example, the *Atrina rigida* specimen was received 5<sup>th</sup>, thus the PEEM-analyzed sample is labeled: Ar5-1, and the clumped isotope-analyzed sample is labeled Ar5-2. In all figures in this work, however, the last hyphen and number are omitted for simplicity. Associated specimen information is archived in a nacre sample compendium on:

[http://home.physics.wisc.edu/gilbert/nacre/sample\\_compendium.html](http://home.physics.wisc.edu/gilbert/nacre/sample_compendium.html). [Table S1](#) contains a summary of specimen information and [Figures 8, 9, S11](#) provide sample collection location and temperature data measured by nearby buoys or weather stations from the recent samples over the lifetime of the organisms (Pc2, Ar5, and Pn1).

**Ar5:** Recent *Atrina rigida* (size: 29 cm along the vertical in [Figure 4, S4](#)). Purchased from Gulf Specimen Marine Laboratory, Panacea, FL, USA. The living animal was collected at the beginning of September 2014 from St. Joseph Bay, Gulf county, FL (29° 43' 15" N / 85° 19' 39" W) from a collection depth of between 0.5 and 2.0m, kept in a tank for 3-4 weeks, shipped live to Madison, WI and sacrificed on Sept. 30th, 2014. The specimen grew in water temperatures ranging between ~10°C and ~32°C (buoy T data in [Figure S11](#)). PEEM sample Ar5-1 was cut from the right valve (RV) of shell Ar5, as shown in [Figure S4](#).

Clumped isotope analysis was performed on the left valve (LV) and named Ar\_5\_a, Ar\_5\_a\_6\_10, Ar\_5\_c. The clumped isotope data from Ar5 were not included because there was major contamination during the analysis, and the results are off by 1000°C.

**Ar3:** Recent *Atrina rigida* (size: 21 cm). Purchased the same day as Ar5 from Gulf Specimen Marine Laboratory, Panacea, FL, USA. In all other respects identical to Ar5 (see [Figure S11](#) for location and buoy T data). The LV was analyzed here only using SEM in [Figure 5](#), and is therefore not included in [Table S1](#), or in the sample counting.

**Pc2:** Recent *Pinna carnea* (size: 22.5 cm). Specimen from the Malacology collection of the Museum of Comparative Zoology (MCZ), Harvard University, Cambridge, MA, USA. Catalog number MCZ 382622: collected by Sarah Lemer on March 15, 2015 in Boca del Drago (9°24'17" N / 82°19'26" W), Isla Colón, Archipelago of Bocas del Toro, Panama ([Figure 8](#)), at a depth of 1-1.5m. Before sacrificing it, the specimen was kept for six days in an outdoor, shaded tank at the Smithsonian Tropical Research Institute (STRI) Marine station under

constant flow of seawater from the coastline at its natural temperature. The specimen grew in water temperatures ranging from ~26°C to ~31°C (Figure 8). The LV was used for both PEEM (Pc2-1) and clumped isotope (Pc2-2) analyses.

**Pn1:** Recent *Pinna nobilis* (size: 28 cm). Also from the Malacology collection of the MCZ, Harvard University, Cambridge, MA, USA. Catalog number MCZ 371544: collected by Juan Giribet in Mallorca, Spain, 1991 (Figure 9). The temperature record from 1990-1991 is unavailable. Temperature records in Figure 9 show the locations where the buoy T data were collected in recent years. The specimen likely grew in water temperatures ranging from ~10°C to ~30°C (Figure 9). The LV was used for both PEEM (Pn1-1) and clumped isotopes (Pn1-2) analyses.

**Ah2:** Miocene *Atrina harrisii* (fragment size: 7 cm). Courtesy of Robert Hazen and John Nance, Calvert Marine Museum Invertebrates Collection, Solomons, MD USA. Catalogue number CMM-I-237: collected from Bed 19, Boston Cliffs Member, Choptank Formation, Chesapeake Group (Middle Miocene Epoch ~12 Ma). The sample appearance and preparation are shown in Figure S7. Fragment size prohibited identification of RV or LV for PEEM (Ah2-1) and clumped isotope (Ah2-2) analyses but both analyses were conducted on the same fragment.

**Ah3:** Miocene *Atrina harrisii* (fragment size: 4.5 cm). Courtesy of Susan Butts and Jessica Utrup, Yale Peabody Museum (YPM), Yale University, New Haven, CT, USA. Catalogue number IP 527493: collected by S. M. Kidwell in Saint Marys Co, MD in 1979. Specimen collected from Unit 5 of the Drumcliff Member, Choptank Formation (Middle Miocene ~13 Ma). For more information, see: <http://peabody.yale.edu/collections/search-collections?ip>. A single fragment (RV/LV unknown) was used for PEEM (Ah3-1) and clumped isotope (Ah3-2) analyses. Species designation determined by the authors and confirmed by John Nance (Calvert Marine Museum of Invertebrates) based on absence of interior sulcus or exterior keel, and comparison to other age-equivalent specimens previously described from the Drumcliffs Member (Glenn, 1904; Kidwell, 1982).

**Ah4:** Miocene *Atrina harrisii* (fragment size: 5.5 cm). Courtesy of Susan Butts and Jessica Utrup, YPM, Yale University, New Haven, CT, USA. Catalogue number IP 527512: collected by S. M. Kidwell in Saint Marys Co, MD in 1978. Specimen collected from the top of Unit 1, Drumcliff Shell Bed, Choptank Formation (Middle Miocene ~13 Ma). For more information, see: <http://peabody.yale.edu/collections/search-collections?ip>. A single fragment (RV/LV?) was used for PEEM (Ah4-1) and clumped isotope (Ah4-2) analyses. Species designation determined by the authors and confirmed by John Nance (Calvert Marine Museum of Invertebrates) based on absence of interior sulcus or exterior keel, and comparison to other age-equivalent specimens previously described from the Drumcliffs Member (Glenn, 1904; Kidwell, 1982).

**Px1:** Eocene cf. *Pinna* sp., (fragment size: 3.5 cm). Courtesy of Susan Butts and Jessica Utrup, YPM, Yale University, New Haven, CT, USA. Catalogue number IP 527489: collected by C. O. Dunbar on Feb. 4, 1966 in Butler Co, AL (Coll. 3). Specimen collected from the Bashi Shell Marl, lower Hatchetigbee Formation (Early Eocene ~54 Ma). For more information, see: <http://peabody.yale.edu/collections/search-collections?ip>. A single fragment (RV/LV?) was used for PEEM (Px1-1) and clumped isotope (Px1-2) analyses.

**Px2:** Eocene cf. *Pinna* sp. (fragment size: 6 cm). Courtesy of Susan Butts and Jessica Utrup, YPM, Yale University, New Haven, CT, USA. Catalogue number IP 527490: collected by C. O. Dunbar on Feb. 4, 1966 in Butler Co, AL (Coll. 3). Specimen collected from the Bashi Shell

Marl, lower Hatchetigbee Formation (Early Eocene ~54 Ma). For more information, see: <http://peabody.yale.edu/collections/search-collections?ip> . A single fragment (RV/LV?) was used for PEEM (Px2-1) and clumped isotope (Px2-2) analyses.

**Ps5:** Late Cretaceous (Maastrichtian) *Pinna* sp. (fragment size: 8 cm). Courtesy of Neil Landman and Bushra M. Hussaini, American Museum of Natural History (AMNH), New York, NY, USA. Catalogue number 99982: collected by Neil Landman, Susan Klofak, Matt Garb, Remy Rovelli, and Corinne Myers on May 28, 2010 in Tippah, Co, MS. Specimen collected from the Owl Creek Fm, Selma Group (Maastrichtian ~66 Ma). Accessioned specimen consists of many shell fragments; two separate fragments were used for Ps5 and Ps6 below. A single fragment (RV/LV?) was used for PEEM (Ps5-1), clumped isotope (Ps5-2a, Ps5-2c), and EPMA (Ps5-4) analyses. By comparison with *Pinna laqueata* specimens found at this site at the same time and those previously observed in the Owl Creek of Missouri (Stephenson, 1957), it is possible that this shell species was *Pinna laqueata*.

**Ps6:** Late Cretaceous (Maastrichtian) *Pinna* sp. (fragment size: 4 cm). Courtesy of Neil Landman and Bushra M. Hussaini, AMNH, New York, NY, USA. Specimens from same catalogue number, locality, and stratigraphic interval as Ps5 above. A single fragment (RV/LV?) was used for PEEM (Ps6-1) and clumped isotope (Ps6-2a, Ps6-2c) analyses. As for Ps5, it is possible that Ps6 is *Pinna laqueata*, as other *P. laqueata* specimens were found at this site (Stephenson, 1957).

**Pfo1:** Early Jurassic (Pliensbachian) *Pinna folium* (remaining shell size: 12 cm, estimated total size including missing umbo: 15 cm), from Blockley, Gloucestershire, UK, extracted from the Lower Lias. Courtesy of Steven Davies, Dinosaurland Fossil Museum collection, Lyme Regis, Dorset, United Kingdom. The shell shows excellent iridescence, and does not have any calcite prismatic layer in the areas analyzed with SEM. It does not have the umbo anymore. The two valves are closed and filled with calcite, identified by PEEM analysis. A 1cm thick slice was embedded and cut as close to the umbo as possible (~3 cm from it), embedded, polished, and analyzed with SEM. The best region (position 3) was cut, re-embedded and polished for PEEM analysis (Pfo1-3)(Figure S8). No clumped isotope analysis was done as this specimen occluded extensive calcite crystals between the two valves (see top of transects in Figure 6), and the nacre layer was too thin (300  $\mu\text{m}$  at most) for safe, uncontaminated separation.

**Ps8:** Early Jurassic (Pliensbachian) *Pinna folium* (remaining shell size: 5.6 cm, estimated total size including missing umbo: 7 cm), from Blockley, Gloucestershire, UK, extracted around the year 2000 from the Northcott Brick works, Ibex zone, *Beanicerus luridum*. Courtesy of Christopher Andrew, Lyme Regis Museum, Lyme Regis, Dorset, United Kingdom. The shell shows limited iridescence only in one region, and from SEM and PEEM analysis does not have any calcite prismatic layer preserved. It does not have the umbo anymore. The two valves are closed and filled with polycrystalline calcite (from PEEM analysis), the entire specimen was embedded, cut, polished, and analyzed with SEM. The best region (position 2) was cut, re-embedded and polished for PEEM analysis (Ps8-2)(Figure S8). No clumped isotope analysis was done as this specimen had extensive calcite crystals between the two valves, outside of the nacre layer, in between the nacre layer, and even percolating through some of the nacre tablets (see Figure 2F). The nacre layer was even thinner than in the Pfo sample, with 90  $\mu\text{m}$  maximum thickness.

## Sample preparation

Three recent and seven fossil specimens were acquired from the sources described above. The three recent shells were rinsed in ethanol, air-dried, and cut with a jeweler's saw along the bisector line. A second cut, shown in [Figure S4b](#), isolated a shell fragment ~1cm-wide including the thickest nacre (red arrows in [Figures 4, S4, S7](#)) at its center. This sample was then embedded in epoxy to expose the cross-section in the thickest nacre region, polished, and coated. The thickest nacre region was chosen because it provides the most sample to measure, and was deposited over the longest period of time. Consequently, experiments in this region maximize the environmental information stored in each specimen.

Fossil Pinnidae shells are extremely fragile, as shown by the shell fragments at the right hand side of [Figure S7a,b](#) for specimen Ah2. These fragments were cut off for clumped isotope analysis using a razor blade gently pressed through the soft, flaky nacre. Subsequently the remaining specimen was embedded in epoxy, then cut using a diamond saw as shown in [Figures S6 and S7c,d](#). Fossil specimens were then re-embedded to expose a shell cross-section in the region of thickest nacre (missing cuboid in [Figure S6 and S7c,d](#)), polished, and coated similar to recent specimens.

The embedding epoxy in all cases was EpoFix (EMS, Hatfield, PA, USA), poured around the shell fragment in 1-inch round molds, and cured for 13 hours. Before embedding, extreme care was taken to coarsely polish each shell to obtain a flat cross-section perpendicular to the shell inner surface. The specimen was then mounted on double-stick tape to the bottom of the embedding mold in order to minimize any orientation error introduced during the embedding stage. The finished shell mount contained nacre layers perpendicular to the polished surface within an angle of  $\pm 5^\circ$ , thus the mounting error on TT measurements was negligible.

Shell mounts were polished with coarse grit, followed by 300-nm  $\text{Al}_2\text{O}_3$  nanoparticles, followed by 50-nm  $\text{Al}_2\text{O}_3$  nanoparticles (MasterPrep, Buehler, Lake Bluff, IL, USA) suspensions. Before use, both polishing suspensions were dialyzed against 22g/L  $\text{Na}_2\text{CO}_3$  in DD water for 24h with three  $\text{Na}_2\text{CO}_3$  solution changes. The polished samples were rinsed in ethanol, air-dried, covered with a mask in the area to be analyzed (purple square in [Figure S4d](#), transparent square in [Figure S7e](#)), and coated with 40nm Pt. This produced the high-reflectivity region all around the square, (the white region in [Figure S4d](#) and black region in [Figure S7e](#)). The mask was then removed, and the entire sample surface was coated again with 1nm Pt, while rotating the sample. One nm is sufficient to ensure good conductivity, but is less than the ~5 nm depth below the sample surface from which the secondary electrons detected in a PEEM experiments originate ([Frazer et al., 2003](#)). Hence the majority of the detected signal comes from the sample, not the coating. One nm Pt, however, is not enough to make good electrical contact, motivating the thicker coating surrounding the area of interest. One nm coating must be done using a high-precision sputter coater that enables slow, precise coating, during which the sample is tilted and spun (208HR High Resolution Sputter Coater, Cressington, UK, and Ted Pella, Inc., USA). The differential-thickness resulting from two rounds of Pt coating makes it possible to perform photoemission experiments on shells, minerals, rocks, or any other insulators, and was introduced by our group ([De Stasio et al., 2003](#); [DeVol et al., 2014](#)). It also prevents any

charging phenomena or artifacts (Gilbert et al., 2000). Figure S7e shows a polished, trimmed, and coated sample, ready for PEEM analysis.

Sample powders were prepared for clumped isotope analyses from the epoxy-embedded shell fragments surrounding the PEEM sub-sample for Ah3-2, Ah4-2, Px1-2 and Px2-2. A bulk sample of nacre was removed from the epoxy and powdered using a mortar and pestle. For Ah2-2, a subsample from the fragments produced while cutting the sample with a razorblade was powdered with a mortar and pestle. Unembedded samples of Ar5, Pc 1-2, Pn 2-2, Pl-5-2 and Pl-6-2 allowed separation of the prismatic calcite layer and the nacre using a razor blade. Both were powdered using a mortar and pestle prior to clumped isotope analysis.

### **XRD Analysis**

X-ray diffraction patterns (XRD) were collected on beamline 12.3.2 at the Berkeley Advanced Light Source, as described previously, using a DECTRIS Pilatus 1 M area detector (Gilbert et al., 2008; Tamura and Gilbert, 2013; Yang et al., 2011). A  $\sim 1\text{-}\mu\text{m}$  spot, 9 keV monochromatic beam illuminated the sample surface in the locations shown in Figure S2. Each pattern of reflections was indexed using the XMAS software (Tamura, 2014), with excellent calcite and aragonite recognition.

### **SEM Analysis**

For scanning electron microscopy (SEM) analysis, the anterior regions of three recent shells were cut, rinsed with ethanol, air-dried, and coated with 20-nm Pt. The Hitachi S-3400N scanning electron microscope in the UW-Madison Department of Geoscience was used to produce the images in Figure 5, under the secondary-electron mode and an accelerating voltage of 15 kV.

### **EPMA analysis**

Electron Probe Micro-Analysis (EPMA) was conducted to obtain quantitative elemental spot analysis and elemental mapping on the shell Ps 5-4 to assess trace metal variability across the shell. EPMA was done on the JEOL JXA-8200 Electron Microprobe at the California Institute of Technology. For all quantitative results, the accelerating voltage was 15 kV, the beam current was 20 nA, and the beam size was 1  $\mu\text{m}$ . The CITZAF method was used for matrix correction. Sample standards for the five chemical elements analyzed, included: dolomite for Mg, siderite for Fe, rhodochrosite for Mn, strontianite for Sr, and anhydrite for S. Mg had an average detection limit of 0.01% Fe–272 ppm, Mn–388 ppm, Sr–438 ppm, and S–0.02%. EPMA results are presented in Figure S3 and reported in Table S3. The Late Cretaceous shell Ps5 is also extremely well preserved chemically. EPMA measurements, both maps and transects, indicate that Fe and Mn trace metal concentrations are extremely low across the shell (aragonite [Fe] =  $110 \pm 12$  ppm and [Mn] =  $90 \pm 10$  ppm; calcite [Fe] =  $202 \pm 42$  ppm and [Mn] =  $93 \pm 27$  ppm, mean  $\pm$  std. error of the mean). As both metals tend to incorporate into calcite and aragonite in reducing environments below the sediment-water interface, this suggests minimal diagenesis (Brand and Veizer, 1980). Sr and Mg are consistent with primary precipitation of the two phases from seawater (aragonite [Sr] =  $2567 \pm 71$  ppm and [Mg] =  $134 \pm 33$  ppm; calcite [Sr] =  $986 \pm 38$  ppm and [Mg] =  $3909 \pm 187$  ppm) (Figure S3, Table S3).

### Detailed description of digital ruler measurements

Each PIC-map was opened in Adobe Photoshop®, then immediately duplicated into a second “Photoshop layer”. This second layer was then rotated until the nacre tablets were horizontal. Tilt in the other direction was prevented with accurate sample mounting, perpendicular to the polishing and imaging plane. A vertical un-rotated digital ruler with ticks and numbers was pasted into a third “Photoshop layer”. For all images, the digital ruler was arranged such that the “0” tick was located precisely at the bottom of the un-rotated PIC-map. All other ticks were then moved so that each coincided with the boundary between two nacre tablets. In [Figure S9](#) the three “Photoshop layers” are displayed for each PIC-map: at the bottom is the un-rotated original PIC-map layer, on top of it is the rotated PIC-map, and on top of both is the digital ruler, with its white ticks and numbers. Note that “0” is at the bottom of the field of view, and all other ticks and numbers were shifted up or down, one at a time, such that they coincided with nacre tablet boundaries. The vertical-FoV was 21.5  $\mu\text{m}$  in all panels of [Figure S9](#). Note that in [Figure S9](#) we displayed a larger field of view to include all of the un-rotated images. During the measurement the file size was not (and should not be) increased, so the FoV measurement remained the same, even when a Photoshop layer was rotated. This avoids the introduction of any quantitative errors. To obtain the “average TT” in each PIC-map ([Figure S10](#)) we divided the vertical-FoV in each image by the number of tablets counted in that image using the digital ruler. All PIC-maps were measured twice, by two co-authors, recording the results in two separate columns of a Microsoft Excel® spreadsheet. The averages and standard deviations were calculated in Excel®, all the plots were produced in Kaleidagraph® 4.5.2 for Mac.

### Angle spread measurement

The angle spread of  $c'$ -axes (the projections of  $c$ -axes onto the polarization plane of the illuminating radiation) was measured using the “Polarization Analysis Package” of GG Macros ([GG-Macros, 2015](#)). For every PIC-mapped area, we made a polarization stack of 19 images, with linearly polarized illumination covering a range of  $90^\circ$  with a  $5^\circ$  step. By fitting the intensity of a pixel as a function of polarization to [Equation 1](#) (see PIC-mapping), we then determined the values of  $c'$ , the  $c'$ -axis angle, and  $b$ , the amplitude of polarization-dependent intensity, for every pixel in a PIC-mapped area.

To remove artifacts before measurement, we first masked off pixels with extreme values of  $b$ , namely those falling into bins populated by less than  $10^2$  pixels on a histogram of all  $b$ -values from the PIC-map. In particular, this removes artifacts with low polarization-dependence and correspondingly low values of  $b$ .

We then placed the  $c'$ -values of all remaining pixels on a histogram and measured the range of these  $c'$ -axis angle bins that were each occupied by at least  $10^3$  pixels. This somewhat arbitrary occurrence cut-off was used to further ensure that remaining  $c'$ -axis angles, still representing the majority of the  $10^6$  pixels in the image, are not artifactual. Great care was taken to confirm that no real nacre tablets were completely excluded from the AS analysis by this cut-off. The measured angle spread in each PIC-map was always between  $10^\circ$  and  $30^\circ$  for all areas analyzed in recent and fossil nacre, with the only six exceptions due to diagenesis and shown in the six panels of [Figure 2](#).

Using the GG Macros ([GG-Macros, 2015](#)), this analysis of a given PIC-map can be done by following a few simple steps:

- 1) Having opened the experiment file, stacked the 19 images, and produced a PIC-map, now click on the “Analyze output” button in the “Polarization Panel”.
- 2) The “Polarization Result Analysis” panel appears. In that panel, press “Create Masked PICmap”. When you do that, make sure that box “From POL B” is checked in the “Masking” section of the panel: that masks off pixels with extreme  $b$ -values, with  $<10^3$  frequency, as described above.
- 3) A histogram of  $c'$ -values of unmasked pixels appears. Check that the vertical cut-offs are placed at the  $10^3$  level; if necessary, move them manually.
- 4) Click on “Extract Masked AS”. The angle spread is measured and displayed in the command panel.

The average angle spread thus obtained for each shell is shown in [Figure S13](#), and, although extremely noisy, it appears to be anti-correlated with  $T$ . It is possible that this is a sampling artifact: at greater  $T$  tablet thickness is greater, hence there are fewer tablets in the field of view and their possible orientations are under-sampled, resulting in smaller angle spreads. This is confirmed by the shape of  $c'$ -value histograms, which significantly departs from Gaussian at higher  $T$ , and is generally closer to Gaussian at lower  $T$ . Rather than the angle spread in each PIC-map, a measurement of all orientation angles over the entire shell might be more informative, but is beyond the scope of this work.

## 2.7 Abiotic aragonite growth experiment

*Aragonite growth.*—Synthetic aragonite particles were grown simultaneously in sealed Pyrex bowls placed in bio-culture rooms or incubators with different temperatures. The growth solution recipe follows ([Liu et al., 2009](#)). Four 22 mm  $\times$  22 mm glass coverslips were each placed in a 35mm plastic Petri dish containing 3 ml of 10mM  $\text{CaCl}_2$  + 10mM  $\text{MgCl}_2$ . Petri dishes were covered and sealed with Al foil surrounded by Parafilm. Four holes were poked in the Al foil of each dish, using a needle. Each of four covered Petri dishes was placed in a separate sealable 950 ml Pyrex bowl. A chunk of ammonium carbonate ( $\sim$ 8-9 g) was placed on a 35 mm Petri dish with no cover, and put it in each of the Pyrex bowls. The Pyrex bowls were then sealed with plastic covers, and placed in a bowl at one of four different temperatures: 4°C, 15°C, 22°C, and 30°C (4°C and 15°C = “cold” room; 22°C = lab room temperature; 30°C = bacteria plate incubator set to 30°C.). Twenty hours later, each glass coverslip was removed from the growth solution with forceps and rinsed in 10mM Tris, pH 11 for a few seconds, rinsed in 100% ethanol for about 5 seconds, and placed in clean 35mm Petri dishes at an angle resting on the lip of the dish to dry for 1 hour. Dry coverslips were then placed in labeled 50ml screw cap tubes containing Kimwipes to hold the coverslips in place, and transported for imaging.

*Particle size measurement.*—Each coverslip with aragonite particles was imaged using crossed polarizers in reflection mode on a Nikon MM400 visible light microscope. The larger particles grown at 15, 22, 30°C were imaged using the smallest magnification (5 $\times$  objective); the 4°C-particles were imaged with the highest magnification (100 $\times$  objective). Fifteen or more image files were acquired and saved from each sample. Aragonite crystal diameters were measured in Image J<sup>®</sup> using the “straight line selection” tool, after setting

the scale to the appropriate magnification. The green lines shown in **Figure 10** were drawn in Adobe Photoshop® in locations similar to those selected for measurement in Image J®.

### Supporting Information References

- Adamkewicz, S.L., Harasewych, M., Blake, J., Saudek, D., Bult, C.J., 1997. A molecular phylogeny of the bivalve mollusks. *Molec Biol Evol* 14, 619-629.
- Agnini, C., Fornaciari, E., Raffi, I., Rio, D., Röhl, U., Westerhold, T., 2007. High-resolution nannofossil biochronology of middle Paleocene to early Eocene at ODP Site 1262: implications for calcareous nannoplankton evolution. *Marine Micropaleont* 64, 215-248.
- Allen, J.A., 2011. On the functional morphology of *Pinna* and *Atrina* larvae (Bivalvia: Pinnidae) from the Atlantic. *J Marine Biol Assoc UK* 91, 823-829.
- Aucoin, S., Himmelman, J., 2011a. Factors determining the abundance, distribution and population size–structure of the penshell *Pinna carnea*. *Journal of the Marine Biological Association of the United Kingdom* 91, 593-606.
- Aucoin, S., Himmelman, J., 2011b. Factors determining the abundance, distribution and population size–structure of the penshell *Pinna carnea*. *J Marine Biol Assoc UK* 91, 593-606.
- Beer, A.C., Southgate, P.C., 2006. Spat collection, growth and meat yield of *Pinna bicolor* (Gmelin) in suspended culture in northern Australia. *Aquaculture* 258, 424-429.
- Bieler, R., Mikkelsen, P.M., Collins, T.M., Glover, E.A., González, V.L., Graf, D.L., Harper, E.M., Healy, J., Kawauchi, G.Y., Sharma, P.P., 2014. Investigating the Bivalve Tree of Life—an exemplar-based approach combining molecular and novel morphological characters. *Invert Systemat* 28, 32-115.
- Brand, U., Veizer, J., 1980. Chemical diagenesis of a multicomponent carbonate system--1: Trace elements. *J Sedim Res* 50, 1219-1236.
- Butler, A., Brewster, F., 1979. Size distributions and growth of the fan-shell *Pinna bicolor* Gmelin (Mollusca: Eulamellibranchia) in South Australia. *Marine Freshwater Res* 30, 25-39.
- Campbell, D.C., 2000. Molecular evidence on the evolution of the Bivalvia. *Geol Soc Lond Spec Publ* 177, 31-46.
- Cash, W., 1882. Yorkshire Fossil Mollusca, Proceedings of the Yorkshire Geological and Polytechnic Society. Geological Society of London, pp. 77-88.
- Cendejas, J., Carvallo, M., Juárez, L., 1985. Experimental spat collection and early growth of the pen shell, *Pinna rugosa* (Pelecypoda: Pinnidae), from the Gulf of California. *Aquaculture* 48, 331-336.
- Dance, S.P., 2013. The encyclopedia of shells.
- De Stasio, G., Frazer, B.H., Gilbert, B., Richter, K.L., Valley, J.W., 2003. Compensation of charging in X-PEEM: a successful test on mineral inclusions in 4.4 Ga old zircon. *Ultramicroscopy* 98, 57-62.
- Dennis, K.J., Affek, H.P., Passey, B.H., Schrag, D.P., Eiler, J.M., 2011. Defining an absolute reference frame for ‘clumped’ isotope studies of CO<sub>2</sub>. *Geochim Cosmochim Acta* 75, 7117-7131.
- DeVol, R.T., Metzler, R.A., Kabalah-Amitai, L., Pokroy, B., Politi, Y., Gal, A., Addadi, L., Weiner, S., Fernandez-Martinez, A., Demichelis, R., Gale, J.D., Ihli, J., Meldrum, F.C., Blonsky, A.Z., Killian, C.E., Salling, C.B., Young, A.T., Marcus, M.A., Scholl, A., Doran, A., Jenkins, C., Bechtel, H.A., Gilbert, P.U.P.A., 2014. Oxygen spectroscopy and Polarization-dependent Imaging Contrast (PIC)-mapping of calcium carbonate minerals and biominerals. *J Phys Chem B* 118, 8449-8457.

- Eiler, J.M., 2007. "Clumped-isotope" geochemistry—The study of naturally-occurring, multiply-substituted isotopologues. *Earth Plan Sci Lett* 262, 309-327.
- Einstein, A., 1905. Generation and conversion of light with regard to a heuristic point of view. *Annalen Der Physik* 17, 132-148.
- En-Zhi, M., Boucot, A., Xu, C., Jia-Yu, R., 1986. Correlation of the Silurian rocks of China. *Geol Soc Amer Special Papers* 202, 1-81.
- Frazer, B.H., Gilbert, B., Sonderegger, B.R., De Stasio, G., 2003. The probing depth of total electron yield in the sub keV range: TEY-XAS and X-PEEM. *Surf Sci* 537, 161-167.
- Frederiksen, N.O., Gibson, T.G., Bybell, L.M., 1982. Paleocene-Eocene boundary in the eastern Gulf Coast. *Gulf Coast Assocn Geol Soc Trans* 32, 289-294.
- GG-Macros, 2015. <http://home.physics.wisc.edu/gilbert/GG-macros>.
- Gilbert, B., Andres, R., Perfetti, P., Margaritondo, G., Rempfer, G., De Stasio, G., 2000. Charging phenomena in PEEM imaging and spectroscopy. *Ultramicroscopy* 83, 129-139.
- Gilbert, P.U.P.A., 2012. Polarization-dependent Imaging Contrast (PIC) mapping reveals nanocrystal orientation patterns in carbonate biominerals. *J Electr Spectrosc Rel Phenom*, special issue on Photoelectron microscopy, Time-resolved pump-probe PES 185, 395-405.
- Gilbert, P.U.P.A., Metzler, R.A., Zhou, D., Scholl, A., Doran, A., Young, A., Kunz, M., Tamura, N., Coppersmith, S.N., 2008. Gradual Ordering in Red Abalone Nacre. *J Am Chem Soc* 130, 17519-17527.
- Gilbert, P.U.P.A., Young, A., Coppersmith, S.N., 2011. Measurement of c-axis angular orientation in calcite (CaCO<sub>3</sub>) nanocrystals using x-ray absorption spectroscopy. *Proc Natl Acad Sci USA* 108, 11350-11355.
- Giribet, G., Distel, D.L., 2003. Bivalve phylogeny and molecular data. *Molec System Phylogeogr Moll*, 45-90.
- Giribet, G., Wheeler, W., 2002. On bivalve phylogeny: a high - level analysis of the Bivalvia (Mollusca) based on combined morphology and DNA sequence data. *Invert Biol* 121, 271-324.
- Glenn, L., 1904. Mollusca, Pelecypoda. *System Paleontol Miocene: Maryland Geological Survey Miocene Volume*, 274-401.
- Grave, B.H., 1911. Anatomy and physiology of the wing-shell *Atrina rigida*. Govt. print. off.
- Hendriks, I.E., Basso, L., Deudero, S., Cabanellas-Reboredo, M., Álvarez, E., 2012. Relative growth rates of the noble pen shell *Pinna nobilis* throughout ontogeny around the Balearic Islands (Western Mediterranean, Spain). *J Shellfish Res* 31, 749-756.
- Henkes, G.A., Passey, B.H., Wanamaker, A.D., Grossman, E.L., Ambrose, W.G., Carroll, M.L., 2013. Carbonate clumped isotope compositions of modern marine mollusk and brachiopod shells. *Geochim Cosmochim Acta* 106, 307-325.
- Hertz, H., 1887. Ueber einen Einfluss des ultravioletten Lichtes auf die elektrische Entladung. *Annalen der Physik* 267, 983-1000.
- Huntington, K., Eiler, J., Affek, H., Guo, W., Bonifacie, M., Yeung, L., Thiagarajan, N., Passey, B., Tripathi, A., Daëron, M., 2009. Methods and limitations of 'clumped' CO<sub>2</sub> isotope ( $\Delta 47$ ) analysis by gas - source isotope ratio mass spectrometry. *J Mass Spectrom* 44, 1318-1329.
- Idris, M., Arshad, A., Bujang, J., Ghaffar, M., Daud, S., 2008. Biodiversity and distribution of pen shells (Bivalvia: Pinnidae) from the seagrass beds of Sungai Pulai, Peninsular Malaysia. *Res J Fisheries Hydrobiol* 3, 54-62.

- Ivany, L.C., 2012. Reconstructing paleoseasonality from accretionary skeletal carbonates—challenges and opportunities, *Reconstructing Earth's Deep-Time Climate—The State of the Art in 2012*, pp. 133-165.
- Joubert, C., Linard, C., Le Moullac, G., Soyeux, C., Saulnier, D., Teaniniuraitemoana, V., Ky, C.L., Gueguen, Y., 2014. Temperature and Food Influence Shell Growth and Mantle Gene Expression of Shell Matrix Proteins in the Pearl Oyster *Pinctada margaritifera*. *PLoS one* 9, e103944.
- Kidwell, S.M., 1982. Stratigraphy, in *Vertebrate Taphonomy and Depositional History of the Miocene Calvert and Choptank Formations, Atlantic Coastal Plain*. Yale University.
- Kidwell, S.M., 1997. Anatomy of extremely thin marine sequences landward of a passive-margin hinge zone: Neogene Calvert Cliffs succession, Maryland, USA. *J Sedim Res* 67, 322-340.
- Killian, C.E., Metzler, R.A., Gong, Y.U.T., Olson, I.C., Aizenberg, J., Politi, Y., Wilt, F.H., Scholl, A., Young, A., Doran, A., Kunz, M., Tamura, N., Coppersmith, S.N., Gilbert, P.U.P.A., 2009. Mechanism of Calcite Co-Orientation in the Sea Urchin Tooth. *J Am Chem Soc* 131, 18404-18409.
- Kim, S.-T., Mucci, A., Taylor, B.E., 2007a. Phosphoric acid fractionation factors for calcite and aragonite between 25 and 75 C: revisited. *Chem Geol* 246, 135-146.
- Kim, S.-T., O'Neil, J.R., 1997. Equilibrium and nonequilibrium oxygen isotope effects in synthetic carbonates. *Geochim Cosmochim Acta* 61, 3461-3475.
- Kim, S.-T., O'Neil, J.R., Hillaire-Marcel, C., Mucci, A., 2007b. Oxygen isotope fractionation between synthetic aragonite and water: influence of temperature and Mg<sup>2+</sup> concentration. *Geochim Cosmochim Acta* 71, 4704-4715.
- Kožul, V., Glavić, N., Bolotin, J., Antolović, N., 2011. The experimental rearing of fan mussel *Pinna nobilis* (Linnaeus, 1758), *Procs 46th Croatian and 6th Internat Symp on Agriculture, Opatija, Croatia*, p. 806.
- Landman, N.H., Johnson, R.O., Edwards, L.E., 2004. Cephalopods from the Cretaceous/Tertiary boundary interval on the Atlantic Coastal Plain, with a description of the highest ammonite zones in North America. Part 2. Northeastern Monmouth County, New Jersey. *Bull Am Mus Nat Hist* 287, 1-107.
- Larina, E.A., 2015. Upper Maastrichtian ammonite biostratigraphy of the Gulf Coastal Plain, *Geology*. Brooklyn College, p. 65.
- Laves, F., 1974. Use of photoemission electron-microscopy (peem) on decomposition features in minerals and other materials. *Amer Mineral* 59, 1136-1137.
- Lemer, S., Buge, B., Bemis, A., Giribet, G., 2014. First molecular phylogeny of the circumtropical bivalve family Pinnidae (Mollusca, Bivalvia): evidence for high levels of cryptic species diversity. *Molec phylog evol* 75, 11-23.
- Linard, C., Gueguen, Y., Moriceau, J., Soyeux, C., Hui, B., Raoux, A., Cuif, J.P., Cochard, J.-C., Le Pennec, M., Le Moullac, G., 2011. Calcein staining of calcified structures in pearl oyster *Pinctada margaritifera* and the effect of food resource level on shell growth. *Aquaculture* 313, 149-155.
- Liu, R., Xu, X., Cai, Y., Cai, A., Pan, H., Tang, R., Cho, K., 2009. Preparation of calcite and aragonite complex layer materials inspired from biomineralization. *Cryst Growth Des* 9, 3095-3099.
- Lowenstam, H.A., Weiner, S., 1989. *On biomineralization*. Oxford University Press.

- Madix, R., Solomon, J., Stöhr, J., 1988. The orientation of the carbonate anion on Ag (110). *Surf Sci* 197, L253-L259.
- Marie, B., Joubert, C., Tayalé, A., Zanella-Cléon, I., Belliard, C., Piquemal, D., Cochenne-Laureau, N., Marin, F., Gueguen, Y., Montagnani, C., 2012. Different secretory repertoires control the biomineralization processes of prism and nacre deposition of the pearl oyster shell. *Proc Natl Acad Sci USA* 109, 20986-20991.
- Matsumoto, M., 2003. Phylogenetic analysis of the subclass Pteriomorpha (Bivalvia) from mtDNA COI sequences. *Molec Phylogen Evol* 27, 429-440.
- Mendo, T., Koch, V., Wolff, M., Sínsel, F., Ruiz-Verdugo, C., 2011. Feasibility of intertidal bottom culture of the penshell *Atrina maura* in Bahia Magdalena, Baja California Sur, Mexico. *Aquaculture* 314, 252-260.
- Olson, I.C., Blonsky, A.Z., Tamura, N., Kunz, M., Gilbert, P.U.P.A., 2013. JOURNAL COVER. Crystal nucleation and near-epitaxial growth in nacre. *J Struct Biol* 184, 454-457.
- Olson, I.C., Kozdon, R., Valley, J.W., Gilbert, P.U.P.A., 2012. JOURNAL COVER. Mollusk shell nacre ultrastructure correlates with environmental temperature and pressure. *J Am Chem Soc* 134, 7351-7358.
- Passey, B.H., Levin, N.E., Cerling, T.E., Brown, F.H., Eiler, J.M., 2010. High-temperature environments of human evolution in East Africa based on bond ordering in paleosol carbonates. *Proc Natl Acad Sci USA* 107, 11245-11249.
- Press, W.H., Teukolsky, S.A., Vetterling, W.T., Flannery, B.P., 1996. Numerical recipes in Fortran 77 and Fortran 90. Cambridge University Press Cambridge.
- Richardson, C., Kennedy, H., Duarte, C., Kennedy, D., Proud, S., 1999. Age and growth of the fan mussel *Pinna nobilis* from south-east Spanish Mediterranean seagrass (*Posidonia oceanica*) meadows. *Marine Biol* 133, 205-212.
- Richardson, C., Peharda, M., Kennedy, H., Kennedy, P., Onofri, V., 2004a. Age, growth rate and season of recruitment of *Pinna nobilis* (L) in the Croatian Adriatic determined from Mg: Ca and Sr: Ca shell profiles. *J Exper Marine Biol Ecol* 299, 1-16.
- Richardson, C., Peharda, M., Kennedy, H., Kennedy, P., Onofri, V., 2004b. Age, growth rate and season of recruitment of *Pinna nobilis* (L) in the Croatian Adriatic determined from Mg: Ca and Sr: Ca shell profiles. *Journal of Experimental Marine Biology and Ecology* 299, 1-16.
- Rosewater, J., 1961. The family Pinnidae in the Indo-Pacific. *Indo-Pacif Mollusca* 1, 501.
- Rosewater, J., 1982. Review of Hawaiian Pinnidae and revalidation of *Pinna exquisita* Dall, Bartsch, and Rehder, 1938 (Bivalvia: Mytiloidea).
- Ruedemann, R., 1916. The Paleontology of Arrested Evolution. *New York State Mus Bull* 196, 107-134.
- Ruedemann, R., 1918. The Paleontology of Arrested Evolution: Address by the President of the Paleontological Society, Albany, December 1916. University of the State of New York.
- Schöne, B.R., 2008. The curse of physiology—challenges and opportunities in the interpretation of geochemical data from mollusk shells. *Geo-Marine Lett* 28, 269-285.
- Schultz, P.W., Huber, M., 2013. Revision of the worldwide recent Pinnidae and some remarks on fossil European Pinnidae. *ConchBooks*, Öhringen, Germany.
- Sessa, J.A., Ivany, L.C., Schlossnagle, T.H., Samson, S.D., Schellenberg, S.A., 2012. The fidelity of oxygen and strontium isotope values from shallow shelf settings: Implications for temperature and age reconstructions. *Palaeogeogr Palaeoclimatol Palaeoecol* 342, 27-39.

- Steiner, G., Hammer, S., 2000. Molecular phylogeny of the Bivalvia inferred from 18S rDNA sequences with particular reference to the Pteriomorpha. *Geol Soc Lond Spec Publ* 177, 11-29.
- Stephenson, L.W., 1957. A Shorter Contribution To General Geology. *Geol Survey Profess Paper* 274, 97.
- Stohr, J., Wu, Y., Hermsmeier, B.D., Samant, M.G., Harp, G.R., Koranda, S., Dunham, D., Tonner, B.P., 1993. Element-specific magnetic microscopy with circularly polarized x-rays. *Science* 259, 658-661.
- Strack, E., 2001. Pearls. *Rühle-Diebener*.
- Tamura, N., 2014. XMAS: A versatile tool for analyzing synchrotron X-ray microdiffraction data. *Strain and Dislocation Gradients from Diffraction. Spatially-Resolved Local Structure and Defects; Barabash, R*, 125-155.
- Tamura, N., Gilbert, P.U.P.A., 2013. X-ray Microdiffraction of Biominerals, in: De Yoreo, J.J. (Ed.), *Research Methods in Biomineralization Science* Academic Press, Burlington, MA, pp. 501-532.
- Thibault, N., Gardin, S., 2006. Maastrichtian calcareous nannofossil biostratigraphy and paleoecology in the Equatorial Atlantic (Demerara Rise, ODP Leg 207 Hole 1258A). *Rev Micropaléontol* 49, 199-214.
- Thibault, N., Gardin, S., 2007. The late Maastrichtian nannofossil record of climate change in the South Atlantic DSDP Hole 525A. *Marine Micropaleontol* 65, 163-184.
- Tonner, B.P., Harp, G.R., 1988. Photoelectron microscopy with synchrotron radiation. *Rev Sci Instrum* 59, 853-858.
- Turner, R.D., Rosewater, J., 1958. The family Pinnidae in the western Atlantic. *Johnsonia* 3, 285-326.
- Wheulton, H., 1905. A monograph of the British Carboniferous Lamellibranchiata Volume II. *Palaeontographical Society*.
- Yang, L., Killian, C.E., Kunz, M., Tamura, N., Gilbert, P.U.P.A., 2011. Biomineral nanoparticles are space-filling. *RSC-Nanoscale* 3, 603-609.
- Yonge, C.M., 1953a. Form and habit in *Pinna carnea* Gmelin. *Philosophical Transactions of the Royal Society B: Biological Sciences* 237, 335-374.
- Yonge, C.M., 1953b. Form and habit in *Pinna carnea* Gmelin. *Phil Trans R Soc B: Biol Sci* 237, 335-374.
- Young, A.T., Feng, J., Arenholz, E., Padmore, H.A., Henderson, T., Marks, S., Hoyer, E., Schlueter, R., Kortright, J.B., Martynov, V., Steier, C., Portmann, G., 2001. First commissioning results for the elliptically polarizing undulator beamline at the Advanced Light Source. *Nucl Instr Meth A* 467, 549-552.
- Zachos, J., Pagani, M., Sloan, L., Thomas, E., Billups, K., 2001. Trends, rhythms, and aberrations in global climate 65 Ma to present. *Science* 292, 686-693.
- Zhang, R., 1988. Stratigraphic and paleobiogeographic aspects of Devonian bivalves of China.

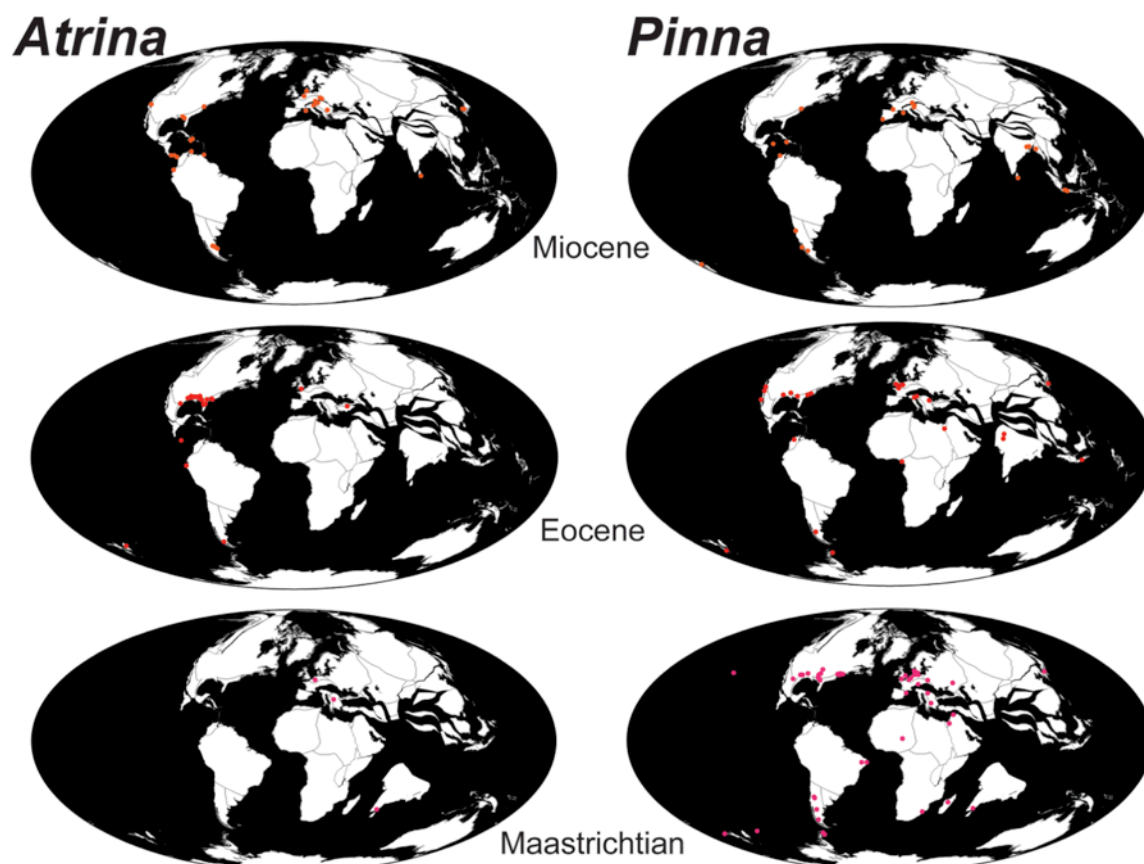


**Figure S1.** Fossil distribution of *Atrina* and *Pinna* during the Miocene, Eocene, and Late Cretaceous epochs. Fossil occurrence data downloaded from the Paleobiology Database on 5/25/15.

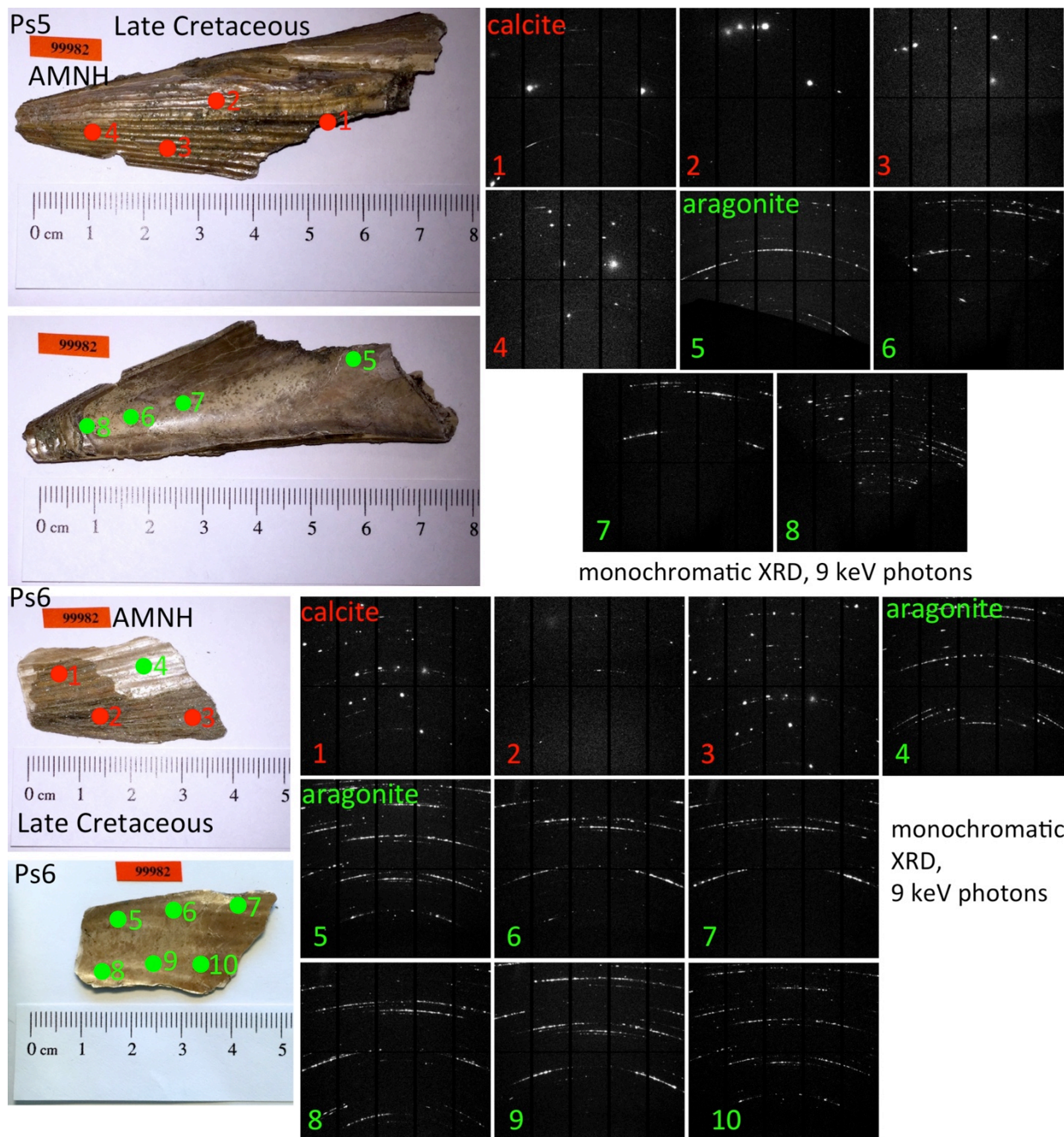


**Figure S2.** X-ray diffraction patterns, obtained from the red and green spots correspondingly numbered on the photographs. Exterior prismatic layer (top) and interior nacreous layer (bottom) photographs are shown. Indexing demonstrates that in red spot locations the mineral is calcite, and in green spots, aragonite.

Ps5 and Ps6 are the two oldest samples in this study, and the only specimens preserving calcite. All other samples contained only aragonite nacre, which was identified as unaltered using spectroscopy at the O K-edge (as in [Figure 1](#)) or at the Ca L-edge ([DeVol et al., 2014](#)).

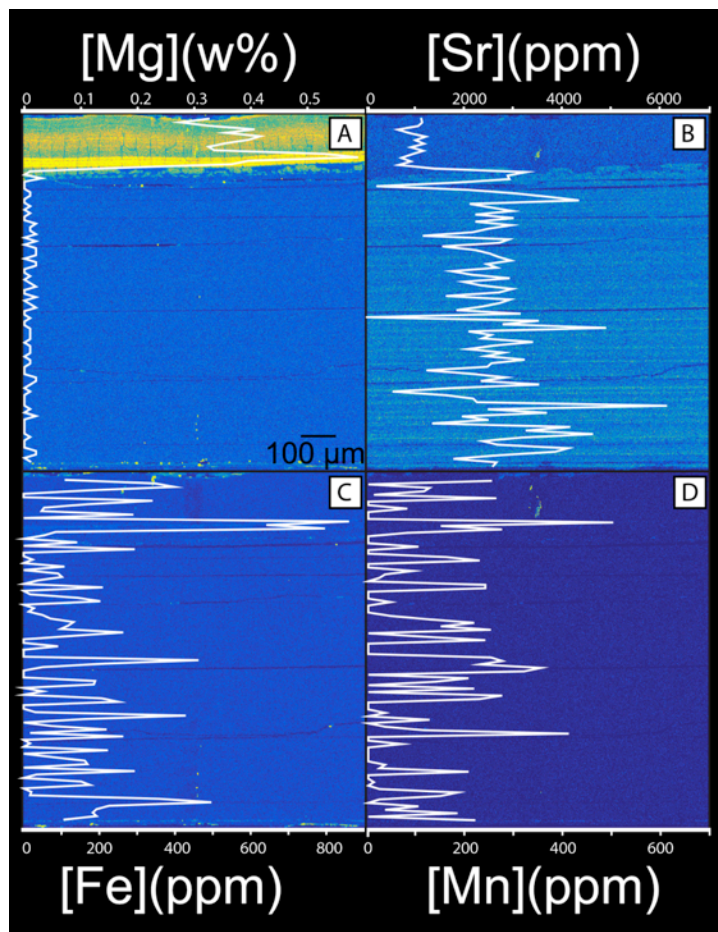


**Figure S3.** EPMA trace metal maps (with warmer colors indicating higher relative concentration) and quantitative transects (white trace) across one shell sample from the Late Cretaceous (Ps5-4). (A) Mg concentration in units of weight %. (B, C, D) Sr, Fe, Mn concentrations in units of parts per million (ppm). Notice in all images the calcite prismatic layer on top, which appears in yellow, as it is Mg-rich, in panel A, and the rest of the image is nacre with occasional horizontal cracks but otherwise homogeneous elemental distributions.

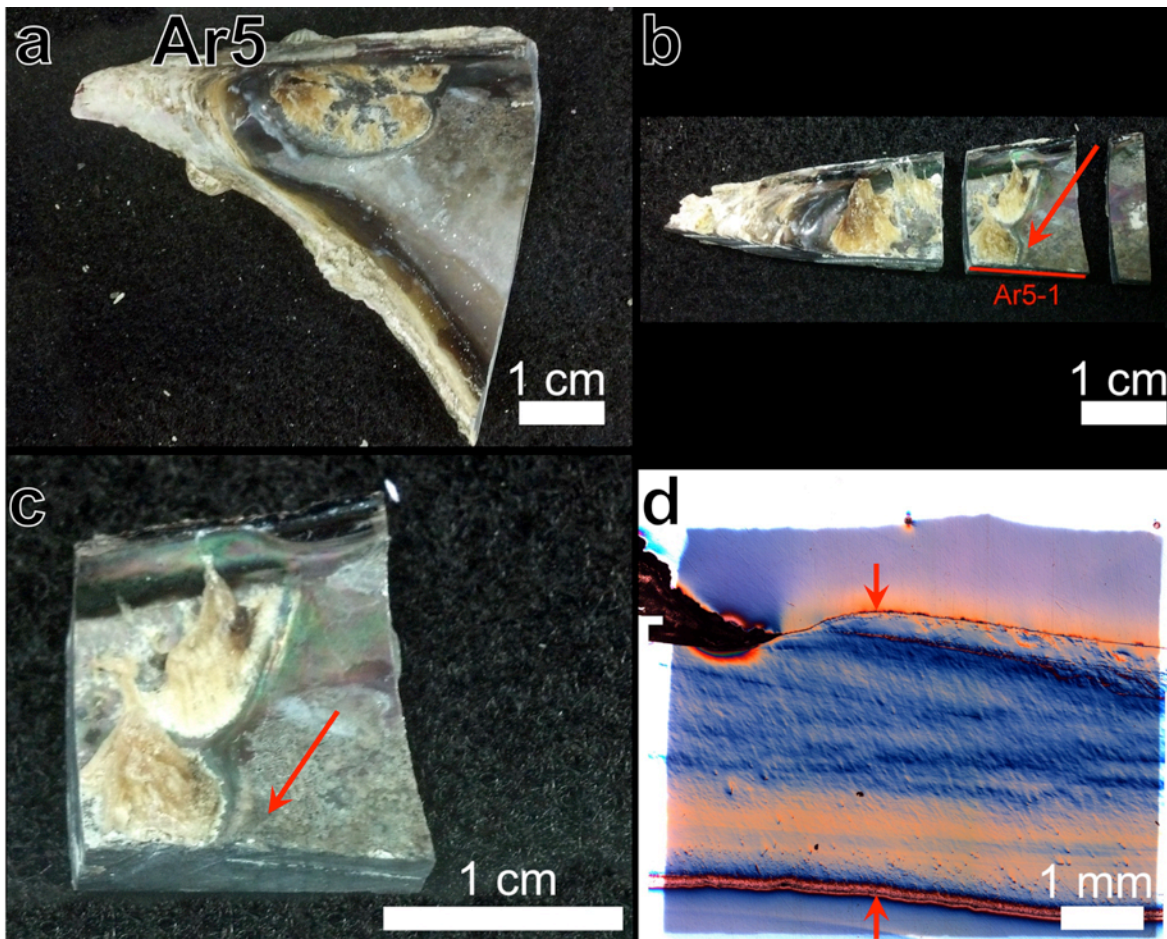


**Figure S4.** The anterior region of Ar5 shell, recent *Atrina rigida*. (a) The umbo is on the left, thickest nacre is just right of the anterior adductor muscle scars (AAs). Note some remaining organic material on the AAs. (b) The same shell after cutting along the bisector line as well as left and right of sample Ar5-1. The red line indicates the side of the shell fragment to be analyzed. (c) Sample Ar5-1 for PEEM analysis, prior to embedding and polishing. The side of the sample at the bottom of the image will be embedded facing down, and polished. Notice the AAs on the left and the thick nacre (red arrows) at the center of the cross-section. (d) Visible Light Microscopy, Differential Interference Contrast (VLM-DIC) micrograph of sample Ar5-1 cross-section, post embedding, polishing and coating, thus ready for PEEM analysis. In this cross-section the interior of the shell is in the upward direction, the umbo to the left. Notice the AAs on the left, appearing as a depression, and some dark, residual organic matter on the AAs. The thickest part of nacre in this cross-section is between the two red arrows. Complete analysis of this cross-section is shown as a series of overlapping PIC-maps in [Figure 6](#).



**Figure S5.** Interior and exterior photographs of the seven fossil specimens analyzed, prior to sample preparation for PIC-mapping. Note that the umbo, AAs, and region of thickest

nacre are well-preserved in most specimens. Whereas all specimens preserve aragonite nacre, prismatic calcite is only preserved in samples Ps5 and Ps6.

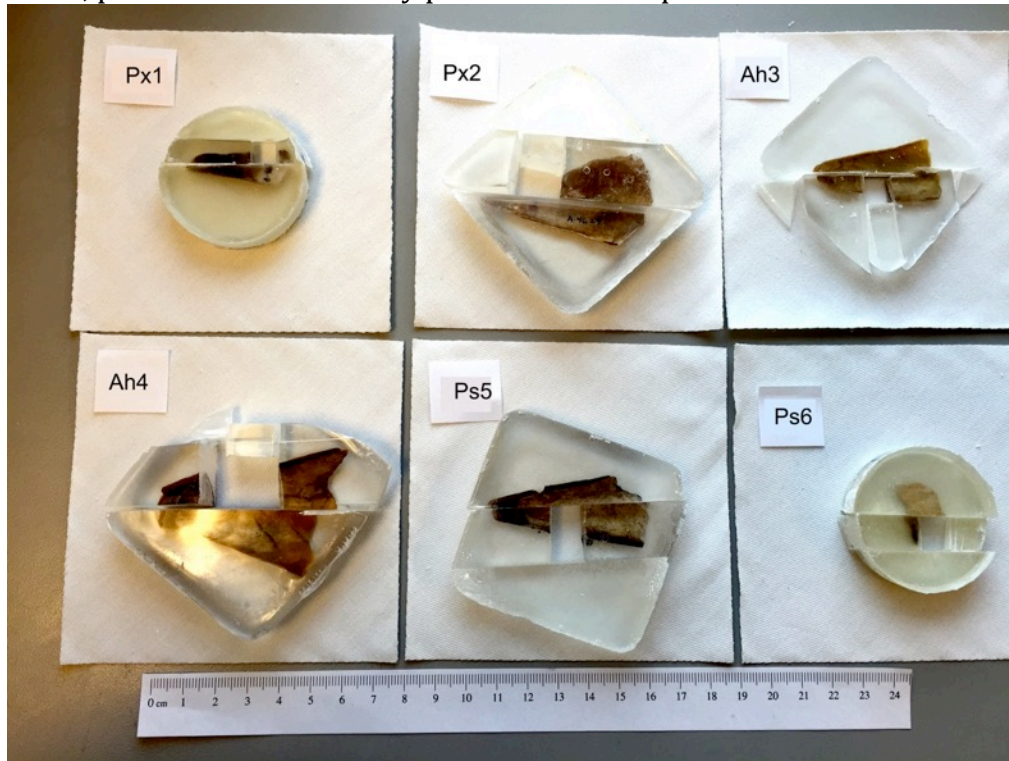


**Figure S6.** Six of the fossil specimens after the first embedding and cutting (see Figure S7 for the 7<sup>th</sup> fossil specimen). All samples are oriented with the interior of the shell facing the reader, and the umbo to the left. The samples analyzed by PEEM are represented by the missing rectangles at the center of each epoxy block. Those are embedded again and polished so the shell transect at the location of thickest nacre is exposed at the center of a flat polished surface, as necessary for the PEEM experiment.

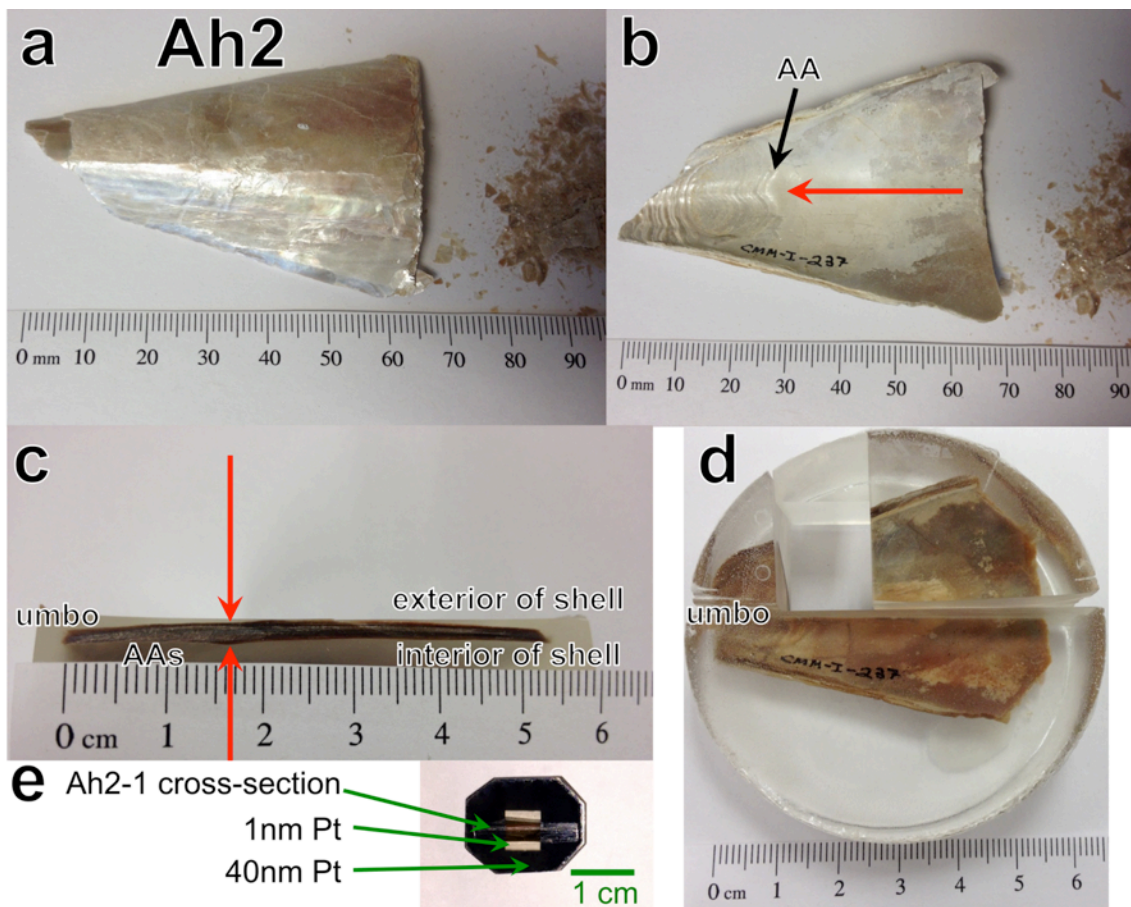


**Figure S7.** Ah2 sample orientation and preparation. Photographs of the Ah2 shell seen from (a) exterior and (b) interior of the shell. Notice the anterior adductor muscle scar (AA) (black arrow in b) and the thickest nacre (red arrows in b and c) posterior to the umbo with respect to the AAs. The embedded shell was cut as shown in d, re-embedded, then polished and coated to obtain the final sample for PEEM analysis shown in e.

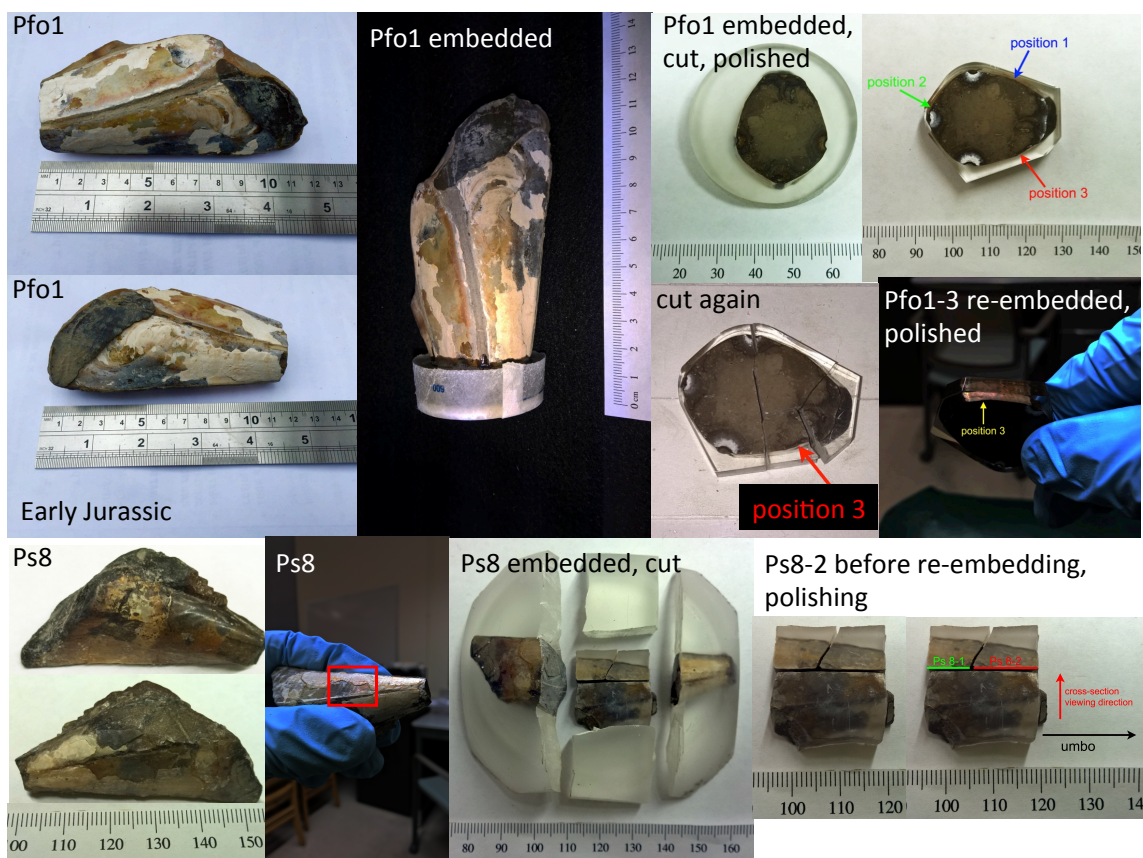


**Figure S8.** Jurassic specimens *Pinna folium* Pfo1 and *Pinna* sp. Ps8, position of samples Pfo1-3 and Ps8-2, and their preparation. The yellow arrow (position 3) and the red square indicate the only two regions that still show iridescence in these two ancient shells.

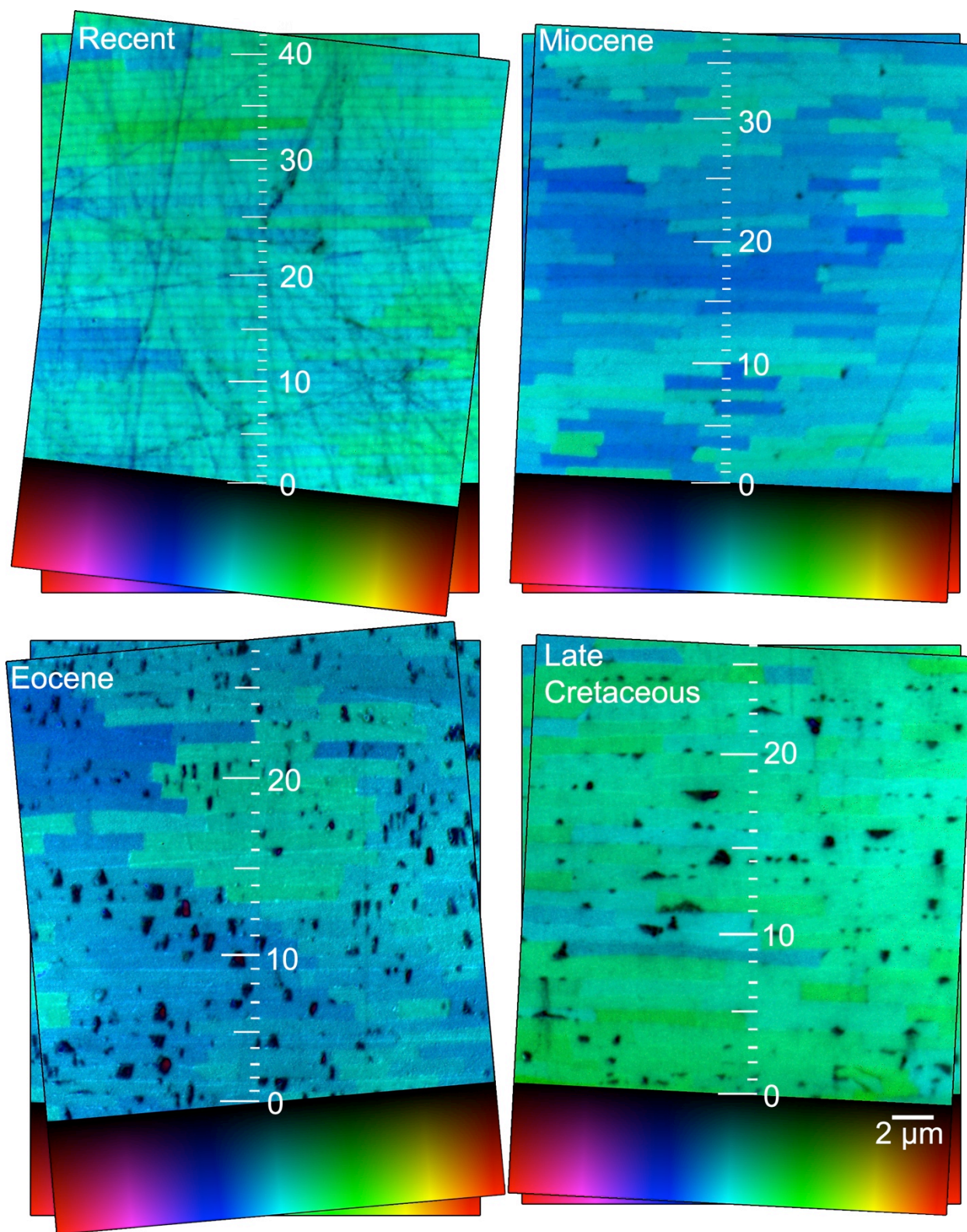


**Figure S9.** PIC-maps of nacre, including color bar c-axis angles, as they are produced using GG macros (GG-Macros, 2015) for four of the specimen areas illustrated in Figure 3. The

samples imaged here are Recent Ar5-1, Miocene Ah4-1, Eocene Px1-1, and Late Cretaceous Ps5-1.

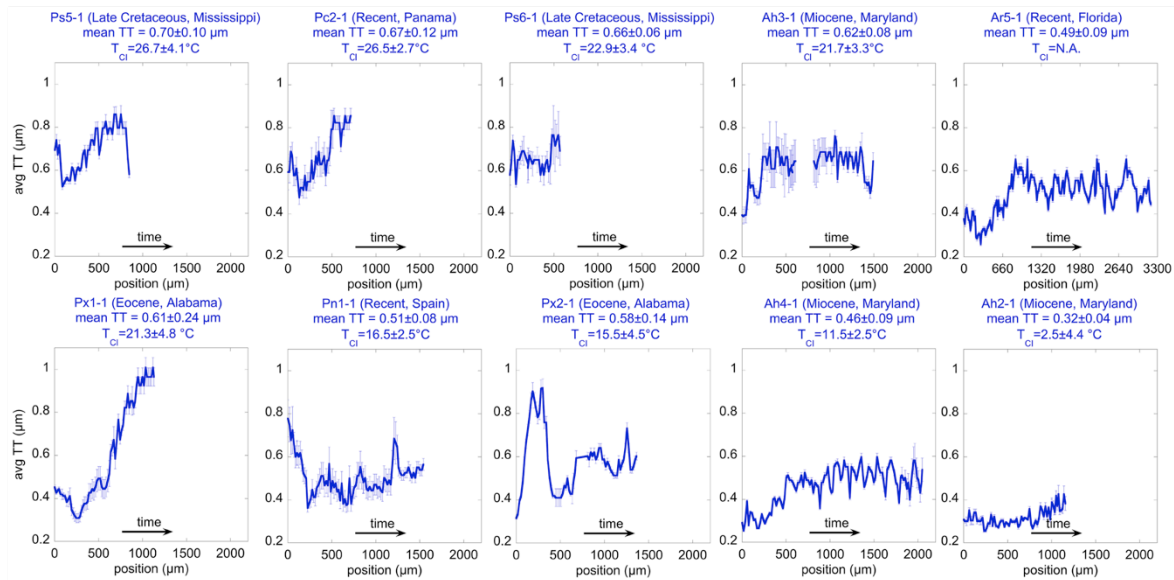


**Figure S10.** Measurements of nacre tablet thickness (TT) vs. position within each specimen cross-section. In all plots, position is 0 at the oldest (first deposited) nacre layer, and it increases across the thickness of the nacre layer, ending at the interior surface of the shell. Consequently, the “position” axis approximates time of deposition directed left (oldest) to right (youngest). The vertical axis is identical in all plots; the horizontal axis ends at 2200  $\mu\text{m}$  in all plots except Ar5-1, where it ends at 3300  $\mu\text{m}$  to accommodate this shell’s thicker nacre layer. The variable in the vertical axis is TT averaged over each image. The mean TT across the entire shell is shown above each plot,  $\pm$  Standard Deviation. The mean clumped isotope (CI) temperature and its standard error of the mean is also shown at the top of each plot. These are the mean TT and T values plotted in **Figure 7A**.

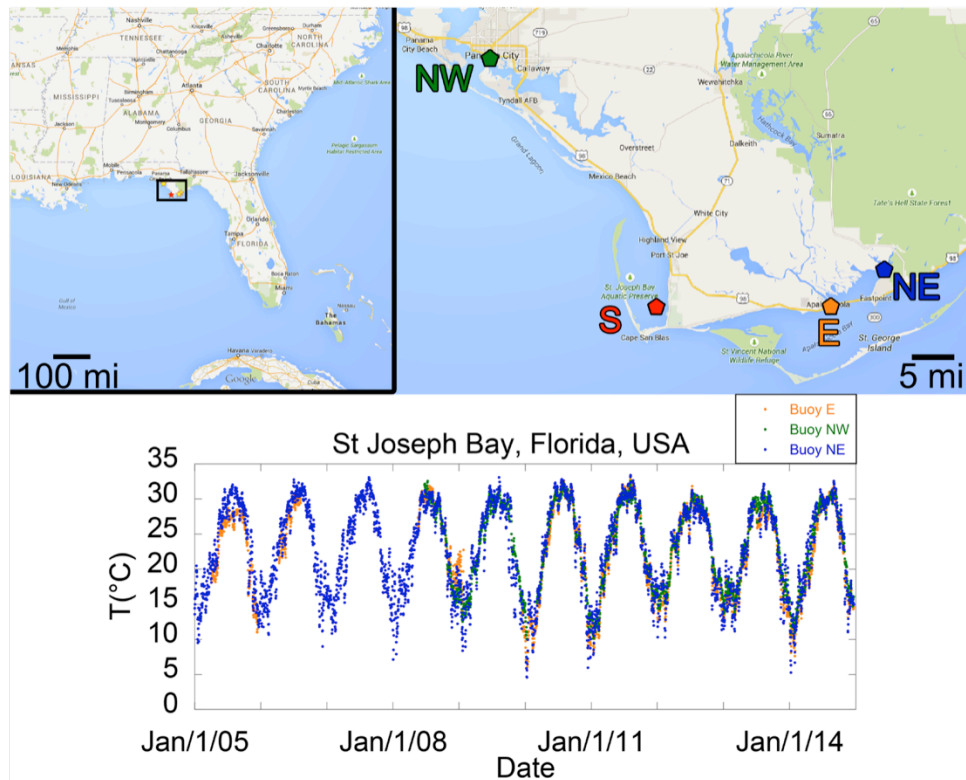


**Figure S11.** Location of Ar5 and Ar3 shell collection. The right-hand map shows the boxed region from the left panel. S = shell collection site: St. Joseph Bay Aquatic Preserve, Florida, USA. Colored pentagons illustrate the location of three marine weather buoys where T data were collected. Buoys are within 60 km of the shell collection location (S), and T measurements show excellent agreement with one another. The data collection and stations are described on [http://www.ndbc.noaa.gov/station\\_page.php?station=pacf1](http://www.ndbc.noaa.gov/station_page.php?station=pacf1), [http://www.ndbc.noaa.gov/station\\_page.php?station=apqf1](http://www.ndbc.noaa.gov/station_page.php?station=apqf1), and [http://www.ndbc.noaa.gov/station\\_page.php?station=apcf1](http://www.ndbc.noaa.gov/station_page.php?station=apcf1). No clumped isotope data were obtained for samples Ar3 and Ar5.

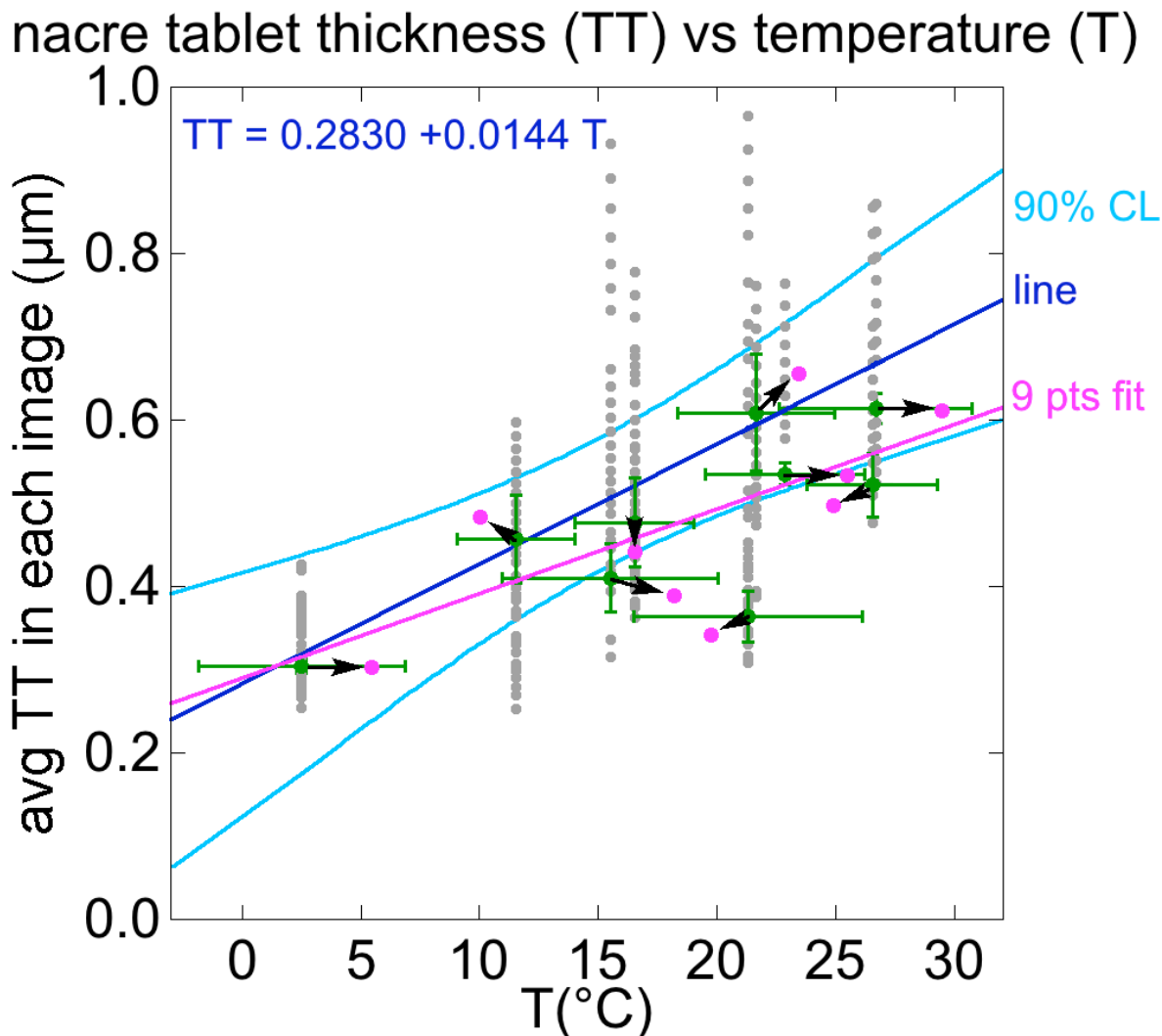


**Figure S12.** Illustration of the method used for fitting data and evaluating confidence limits. All 630 data points from 9 shells are displayed as grey points. For each trial, we randomly select one point from each shell (green dots), then add random deviates (arrows) within the vertical and horizontal error bars, resulting in 9 new data points (magenta dots). We fit these 9 data points (magenta line), and repeat 100,000 times. The centroid of the resulting set of 100,000 fit lines is the most probable estimate (blue “line”) and the 90<sup>th</sup> percentile values are the 90% confidence limits (light blue curves). Error bars for TT measurement, here and in [Figure 7A](#), are 1-5 tablets in each PIC-map, which varied because image quality, sample preservation, and gaps in fossil nacre were all variable across PIC-maps. For T measurements each error bar is one standard error of the mean ( $S. E. M. = 1 \sigma / \sqrt{n}$ , where  $1 \sigma$  is the StDev of n clumped isotope analyses).

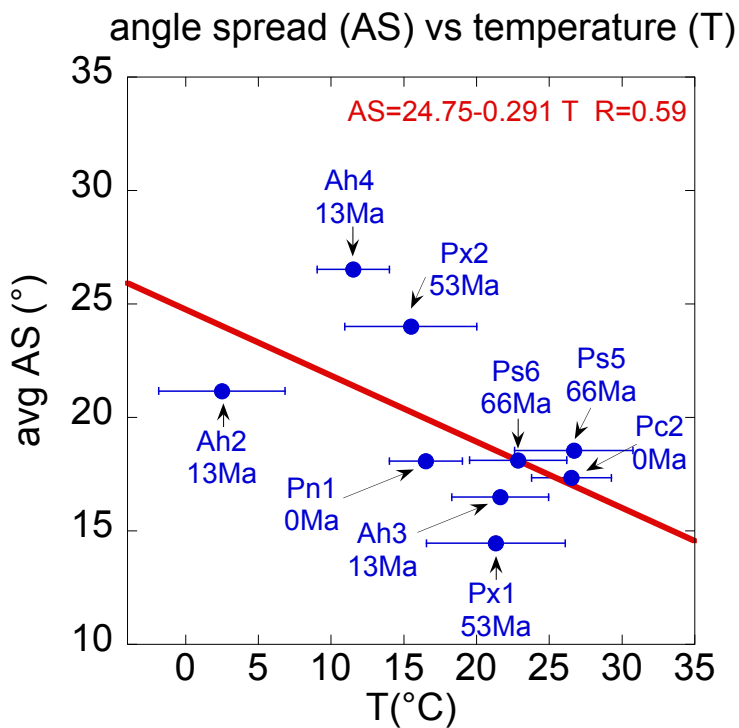


**Figure S13.** Angle spread (AS) measured in each PIC-map, then averaged over the entire shell. T is measured by clumped isotopes. The relationship of AS and T is weaker than for TT and T, but still acceptable. The negative correlation is possibly due to a sampling artifact: with higher T comes greater TT, so there are fewer crystals per PIC-map, and their AS is smaller.

Table S1

PEEM sample ID	Museum ID	Genus and Species	Epoch	Date of Death	Filenames	# Files	avg TT $\pm$ StDev ( $\mu\text{m}$ )	avg AS ( $^{\circ}$ )
Pc2-1	MCZ 382622	<i>Pinna carnea</i>	Recent	03/2015	Pc2-1-156-188 Pc2-1-189-201	46	0.669 $\pm$ 0.115	17.3
Ar5-1	Gulf Specimen	<i>Atrina rigida</i>	Recent	09/2014	Ar5-1-58-91 Ar5-1-92-125 Ar5-1-126-268 Ar5-1-269-301 Ar5-1-302-333 Ar5-1-334-361	192	0.492 $\pm$ 0.087	17.2
Pn1-1	MCZ 371544	<i>Pinna nobilis</i>	Recent	09/1991	P98-196	117	0.506 $\pm$ 0.084	18.1
Ah2-1	CMM-I-237	<i>Atrina harrisii</i>	Middle Miocene	~12.7-13.2 Ma	Ah2-1-168-206 Ah2-1-206-240	81	0.318 $\pm$ 0.039	21.2
Ah3-1	YPM 527493	<i>Atrina harrisii</i>	Middle Miocene	~12.7-13.2 Ma	Ah3-1-48-86 Ah3-1-87-123 Ah3-1-124-136	89	0.617 $\pm$ 0.080	16.5
Ah4-1	YPM 527512	<i>Atrina harrisii</i>	Middle Miocene	~12.7-13.2 Ma	Ah4-1-125-158 Ah4-1-159-191 Ah4-1-192-225 Ah4-1-225-240	110	0.461 $\pm$ 0.089	26.5
Px1-1	YPM 527489	<i>Pinna</i> sp.	Early Eocene	~52-54 Ma	Px1-1-201-232 Px1-1-233-266	66	0.611 $\pm$ 0.242	14.4
Px2-1	YPM 527490	<i>Pinna</i> sp.	Early Eocene	~52-54 Ma	Px2-1-58-84 Px2-1-84-115 Px2-1-115-123	69	0.580 $\pm$ 0.141	24.0
Ps5-1	AMNH 99982	<i>Pinna</i> sp.	Late Cretaceous	~65.5-66 Ma	Ps5-1-04-37 Ps5-1-38-51	48	0.698 $\pm$ 0.100	18.5
Ps6-1	AMNH 99982	<i>Pinna</i> sp.	Late Cretaceous	~65.5-66 Ma	Ps6-1-21-55	40	0.655 $\pm$ 0.055	18.1
Pfo1-2	DFM	<i>Pinna folium</i>	Early Jurassic	~183-191 Ma	T1 P72-79	8	0.586 $\pm$ 0.126	-
Pfo1-2	DFM	<i>Pinna folium</i>	Early Jurassic	~183-191 Ma	T2 P80-88	9	0.619 $\pm$ 0.145	-
Ps8-2	LRM	<i>Pinna</i> sp.	Early Jurassic	~183-191 Ma	P121-123	3	0.486 $\pm$ 0.106	-

**Table S1.** Sample information for the ten *Atrina* and *Pinna* shell samples analyzed in this study. Abbreviations: Gulf Specimen = Gulf Specimen Marine Laboratory, Panacea, FL, USA; MCZ = Museum of Comparative Zoology (MCZ), Harvard University, Cambridge, MA, USA; CMM = Calvert Marine Museum, Solomons, MD, USA; YPD = Yale Peabody Museum of Natural History, Yale University, New Haven, CT, USA; AMNH = American Museum of Natural History, New York, NY, USA; DFM = Dinosaurland Fossil Museum collection, Lyme Regis, UK; LRM = Lyme Regis Museum, Lyme Regis, UK. Filenames correspond to each PIC-map series in [Figure S7](#). An additional recent shell Ar3 (21 cm long) was only used for SEM experiments ([Figure 5](#)) and is therefore not listed in this table.

**Table S2**

Sample ID	Mineralogy	Temperature, °C	Temperature, 1 S.E.M., °C
		Henkes et al., 2012	Carbon Dioxide Equil. Scale
Ah_2	Aragonite	2.51	4.35
Pc_2_2a	Aragonite	26.54	2.73
Pn_1_2a	Aragonite	16.53	2.51
Px_1_2	Aragonite	21.33	4.77
Px_2_2	Aragonite	15.50	4.54
Ah_3_2	Aragonite	21.65	3.33
Ah_4_2	Aragonite	11.54	2.49
Ps_5_2_a	Aragonite	26.70	4.06
Ps_6_2_a	Aragonite	22.87	3.35
Ps_5_2_c	Calcite	23.59	3.41
Ps_6_2_c	Calcite	16.58	1.00

**Table S2.** Clumped isotope data acquired at Caltech in February 2015, and at MIT in June 2015, with excellent reproducibility between standards and replicates run on both mass spectrometers. Here all data are averaged together, with standard error of the mean (S.E.M.) reported in the last column).  $\Delta_{47}$  values are reported in the 'carbon dioxide equilibrium scale' based on theoretical equilibrium values of CO<sub>2</sub> (see Dennis et al., 2011 (Dennis et al., 2011)).

**Table S3**

	Mg (ppm)	Sr (ppm)	Fe (ppm)	Mn (ppm)	S (ppm)
Aragonite Avg.	134	2567	111	90	466
Locations probed	139	139	139	139	139
Std. Error	33	71	12	10	18
Calcite Avg.	3909	986	203	93	1873
Locations probed	21	21	21	21	21
Std. Error	187	38	42	27	195

**Table S3.** Electron Probe Micro-Analysis (EPMA) data acquired along transects of the Late Cretaceous shell Ps5-4. All 139 data points in nacre aragonite and 21 data points in prismatic calcite are displayed in **Figure S3**. Here we only show the averages.